

Humanoid Robot Friction Estimation in Multi-Contact Scenarios

Cameron P. Ridgewell

Thesis submitted to the Faculty of the
Virginia Polytechnic Institute and State University
in partial fulfillment of the requirements for the degree of

Master of Science
in
Mechanical Engineering

Tomonari Furukawa, Co-Chair
Brian Y. Lattimer, Co-Chair
Alan T. Asbeck
Pratap Tokekar

July 25, 2017
Blacksburg, Virginia

Keywords: Robotics, Humanoid Robots, Multi-Contact, Loco-Manipulation, Whole Body
Control, Friction Approximation, Friction Analysis, Multi-Contact Applications
Copyright 2017, Cameron P. Ridgewell

Humanoid Robot Friction Estimation in Multi-Contact Scenarios

Cameron P. Ridgewell

(ABSTRACT)

This paper will present an online approach for friction approximation to be utilized in concert with whole body control on humanoid robots. This approach allows humanoid robots with ankle mounted force-torque sensors to extrapolate information about the friction constraints at the hands during multi-contact poses without the addition of hardware to the platform. This is achieved by utilizing disturbance detection as a method of monitoring active forces at a single external point and deriving available friction force at said contact point in accordance with Coulomb's Law of Friction. First, the rigid body dynamics and required compliant humanoid model optimization are established which allow incorporation of friction constraints. These friction constraints are then informed by monitoring of external forces, which can be used as an indicator of slip based on tangential force. In practice, the robot with operational multi-contact whole body control is navigated to the desired contact surface and normal force only contact is initiated. Using an iterative coefficient estimation based on the achieved system forces, the robot tests the boundaries of its operable force range by inducing slip. Slip detection is utilized as the basis for coefficient estimation, which allows the robot to further understand its environment and apply appropriate forces to its contact points. This approach was implemented on a simple 3 link model to verify expected performance, and then on both the simulated model of Virginia Tech's ESCHER robot and in practice on the actual ESCHER platform. The proposed approach was able to achieve estimation of slip parameters, based largely on time spent measuring, actual friction coefficient, and the available contact force. Though the performance of the proposed approach is dependent on a number of variables, it was able to provide an operational parameter for the robot's whole body controller, allowing expansion of the support region without risking multi-contact slip.

This work was funded by ONR through grant N00014-15-1-2128. HDT Global also supported this project by lending of a pair of Adroit manipulators to Virginia Tech. The author would also like to recognize DARPA for providing the funding to develop the ESCHER platform for the 2015 DARPA Robotics Challenge.

Humanoid Robot Friction Estimation in Multi-Contact Scenarios

Cameron P. Ridgewell

(GENERAL AUDIENCE ABSTRACT)

This paper presents an approach for humanoid robots to use their hands to approximate the friction parameters of contact surfaces without prior knowledge of those parameters. This is accomplished as part of the robot's control system and integrated into its balancing and movement operating system so that it may determine these parameters without ceasing operation. The proposed approach relies on the force sensors typically embedded in the ankles of bipedal robots as its sole force input, so no additional hardware need be added to the robot in order to employ this functionality. Once placed in contact, the robot is able to approximate the forces at its hand with these sensors, and use those approximate values as the basis for estimating the static friction coefficient of the system, in accordance with Coulomb's Law of Friction. The robot's onboard controller is able to utilize this information to ensure that it does not overestimate the available force that may be applied at the contact point, using prior knowledge of the robot model's range of motion. In practice, the robot with this functionality is navigated to the desired contact surface and a hand contact that does not risk slip is initiated. Using an iterative coefficient estimation based on the achieved system forces, the robot tests the boundaries of its operable force range by inducing slip. Slip detection is utilized as the basis for coefficient estimation, which allows the robot to further understand its environment and apply appropriate forces to its contact points. This approach was implemented on a simple 3 link robot model to verify expected performance, and then on both the simulated model of Virginia Tech's ESCHER robot and in practice on the actual ESCHER platform. The proposed approach was able to achieve estimation of slip parameters, based largely on time spent measuring, actual friction coefficient, and the available contact force. Though the performance of the proposed approach is dependent on a number of variables, it was able to provide an operational parameter for the robot's whole body controller, allowing expansion of the support region without risking multi-contact slip.

Acknowledgments

I would like to thank my parents, Brad and Dominique Ridgewell, and my sisters, Caitlin and Brynne for their support and encouragement throughout my education. Without their love and understanding, I would not be the man I am today.

Thanks to my advisors and project leads, Tomonari Furukawa and Brian Lattimer, who provided me the opportunity to work on humanoid robots in the first place. I am very grateful for the guidance, resources, and advice that have been provided to me by their experience.

Thanks as well to Pratap Tokekar and Alan Asbeck for lending their time and wisdom to my research and defense. Thanks as well to Alexander Leonessa for always being willing to contribute to the knowledge and curiosity of the TREC students.

I would also like to thank Peter Amico, George Kontoudis, Jonathon Hodges, Shriya Shah, Murat Ambarkutuk, and all the members of the TREC and CMS Labs here at Virginia Tech for sharing all the highs and lows with me throughout my pursuit of this degree. Thanks as well to Robert Griffin, who acted as another advisor at times, always willing to take the time to explain the software and hardware and to discuss new ideas for research or design.

Thanks as well for the support of my friends, here at Virginia Tech, at Vanderbilt, in Tallahassee, or from anywhere else life has taken me; you have provided me the experience of a lifetime. You have been my inspiration for work and the best cure for life's frustrations. Thanks for everything, Katie, Laura, Karina, Patrick, Dylan, Ryan, Matt, Nate, and all others too numerous to mention.

Finally, I would like to thank Virginia Tech, the Office of Naval Research, and all the students who came before me that for provide this opportunity to work on humanoid robotics in the first place: it has been a dream come true.

Contents

1	Introduction	1
1.1	Bipedal Robots in Context	1
1.2	Integration of Multi-Contact Robotics	2
1.3	Multi-Contact Friction Approximation	2
1.4	SAFFiR Project Overview	3
1.5	Thesis Objectives	4
1.6	Summary of Original Contributions	4
1.7	Thesis Outline	6
2	Literature Review	7
2.1	A Brief History of Humanoid Robotics	7
2.1.1	Bipedal Robot Platforms	7
2.1.2	Development of Bipedal Locomotion	8
2.2	Multi-Contact Humanoids	9
2.3	Friction Approach - Slip Detection and Response	9
3	Overview of Whole Body Control on the Humanoid ESCHER Robot	12
3.1	Hardware Overview	12
3.1.1	Anatomy of the Humanoid ESCHER	12

3.1.2	Upper Body and Hands	14
3.1.3	Lower Body and Feet	14
3.1.4	Additional Sensors	17
3.2	Software Control Hierarchy	17
3.2.1	Motion Manager	17
3.2.2	Communications Manager	20
3.2.3	Momentum Controller	20
3.3	Optimization Based Whole Body Control	21
3.3.1	ESCHER's Rigid Body Dynamics	21
3.3.2	Time-Varying Divergent Component of Motion	21
3.3.3	Task Space Formulation	22
3.3.4	Model Based Optimization based on Time-Varying DCM	23
4	Multi-Contact Momentum Control on the ESCHER Humanoid	25
4.1	Multi-Contact Design Goals	25
4.2	Modification of ESCHER's Momentum Controller	26
4.2.1	Updating the Rigid Body Dynamics	26
4.2.2	Task Space Formulation	27
4.2.3	Expanded Model Optimization	28
4.3	Software Implementation	29
4.3.1	Adaptation of the Momentum Controller Subclass	29
4.3.2	Additional Machine States	30
4.4	Resulting Operation	32
5	Online Multi-Contact Friction Estimation - A Case Study	37

5.1	Significance of Friction Parameters	37
5.2	Formulation of the Friction Estimation Technique	39
5.2.1	Friction Law	39
5.2.2	Force Detection with the Disturbance Model	40
5.2.3	Slip Detection from Applied Force	41
5.2.4	Formulation of the Friction Approximation Technique	42
5.3	Three-Link Simulation	43
5.3.1	Simulation I - Simulation of Different Increment Sizes	45
5.3.2	Simulation II - Increasing the Desired Normal Force	45
5.3.3	Simulation III - Approximation with Similar Coefficients	46
5.4	Implementation on the ESCHER Platform	48
5.4.1	Layout of the Simulation Environment	48
5.4.2	ESCHER Simulation Results	49
5.4.3	Significance of Humanoid Friction Measurements	51
5.4.4	Offline ESCHER Hardware Implementation	52
5.4.5	ESCHER Hardware Setup	52
5.4.6	Establishing Baseline Friction	52
5.4.7	Friction Measurement with the ESCHER Platform	53
5.5	Quantification of Friction Results	54
6	Conclusion and Future Work	58
	Appendix A 2017 IEEE/RAS International Conference on Humanoid Robots	68

List of Figures

3.1	ESCHER platform with 3D printed protective covers. (<i>Photo courtesy of Peter Amico</i>)	13
3.2	An HDT arm is pictured (a) with a closeup of the rubberized palm surface (b)	15
3.3	ESCHER’s right leg is pictured (a) with a closeup of the high friction polymer used on the sole of the right foot (b)	16
3.4	The Motion Manager handles the motion control Finite State Machines that house the interface to the whole body controller. Control messages are communicated to the Comms Manager, informed by proprioceptive messages from the instruments.	18
3.5	Friction pyramids, \mathcal{P}_i , are inscribed in friction cones, \mathcal{C}_i , at the bounding corners of each foot. The generalized forces $\boldsymbol{\rho}_i$ operate within these pyramids to avoid friction limits	23
4.1	Friction cone and friction pyramid distributed representations of localized end effector contact points on palm (left) and foot (right) [1]	33
4.2	The state machine dictates operational parameters and admissible inputs for the robot at any given time. This allows a safe transition to and from the multi-contact states by having them travel through the <code>locomotion_stand_manipulate</code> state	34
4.3	ESCHER approaches the box (a), extends a hand and initiates contact via pre-programmed teleoperation (b-c). With multi-contact functionality enabled, the robot is able to shift its center of mass closer to the platform and utilize its new contact point for stability (d).	35

4.4	The robot begins in a multi-contact pose (a). When the support is suddenly removed, the weight being placed on the robot causes a brief downward lurch (b), before slip is detected. Once slip is detected, the robot reorients to a balanced pose without multi-contact (c)	36
5.1	With added multi-contact support, the COM can be statically moved outside the base support polygon of the feet (b) to anywhere within the contact points established by the feet and hands (a). However, in the orientation specified, the polygon can be expanded using multi-contact and normal forces (c), but some areas of the support polygon are unreachable statically without use of tangential forces at the hand contact location (d)	39
5.2	Illustration of humanoid robot contact frames [1].	41
5.3	A simple 3-link model was developed to simulate a robot with fixed base \mathcal{B} pushing on a non-gravity normal surface at the end effector, \mathcal{E} [1].	44
5.4	The blue lines indicate the desired F_T for each set of force increments, k . Increasing the step size results in less accuracy in the measurement, though execution time is significantly decreased. In general, all three values of k manage to come within 10% of the actual value of μ_s	45
5.5	The blue lines indicate the desired F_T for each set of force increments, k . Increasing the step size results in less accuracy in the measurement, though execution time is significantly decreased. In general, all three values of k manage to come within < 2% of the actual value of μ_s	46
5.6	The blue lines indicate the desired F_T for each set of force increments, k . Operating with 5 N of normal force, and the lowest μ_s of all the simulations, this test resulted in the most inaccuracy across all step sizes. Inaccuracy is somewhat mitigated by the proximity of μ_s and μ_k , and the tendency of this algorithm is to underestimate rather than overestimate, so inaccuracies still will not cause slip.	47
5.7	ESCHER's hand is moved laterally away from the body to apply tangential force to the contact surface.	48

5.8	In the ESCHER Simulation, the maximum F_T achieved was 7.04 N (top). Though the setpoint force for F_N force was 15 N, at the maximum value of F_T , just before 4.5 s, the normal force was measured at, 14.64 N for a calculated $\mu = 0.481$, compared to the actual value, 0.500	49
5.9	Maximum friction coefficient is continuously calculated based on the measured F_T and Equation 5.3.	50
5.10	Not all measurements were consistently clean, with potential stick slip behav- iors challenging the maximum F_T measured. The maximum F_T here is 6.35 N for a μ_s of 0.429 at a k of 2 N.	51
5.11	The palm plate (bottom right) slides down a sheet of wood at 0.712 rad (40.8°) for a measured friction coefficient of $\mu_s = 0.863$	53
5.12	54
5.13	In a tangential force reliant posture (a), the rigid body representation of the robot's applied forces may extend its center of mass, \mathcal{C} , past the ends of its feet, \mathcal{B} , along the x -axis if the moment induced about this point of rotation by the end effector \mathcal{E} from force F_T is greater than or equal to the moment created by the rotation of \mathcal{C} about \mathcal{B}	55
5.14	56

List of Tables

3.1	Mapping of the Behavior and Motion States in the ASGARD Motion System	19
5.1	Results of 3 Link Simulation(Figures 5.4, 5.5, and 5.6)	47

Chapter 1

Introduction

1.1 Bipedal Robots in Context

The face of modern robotics has evolved beyond traditional fixed-base robots in the wake of continued research into floating-base systems. Robots that can move freely through an environment, traverse rough terrain, and properly function in complex or even hazardous conditions provide exciting potential to many fields of research and industry. While many platforms tend more toward wheels and treads, these robots often perform poorly in complex unstructured environments, especially when compared to their legged counterparts [2]. Indeed, though most wheeled platforms do not need to address the complexities of fall prevention, they also encounter a great deal of difficulty navigating common elements in human environments including stairs, narrow hallways, and raised door frames to name a few.

A humanoid robot is theoretically capable of addressing all of these scenarios with the same ease and efficiency as the human for whom such structures were designed. It is due to this versatility that bipedal platforms continue to garner the focus of modern robotics. However, it is not merely the prospect of legged locomotion that gives humanoid platforms the advantage over many other designs. As manipulator technology has become more compact and dexterous, the potential operations of a platform with torso-mounted manipulators are synonymous to humans' own abilities to utilize tools and interact with environments. If humanoid robots are ever to become as ubiquitous as the robotics community anticipates, they will need to properly integrate reliable control schemes and perception capabilities [3].

As bipedal robots broach the infantile stages of venturing beyond laboratory environments, the on-board control systems need to continue to push the limits of the adaptability of their hardware.

1.2 Integration of Multi-Contact Robotics

Though humanoid robots have been studied for decades, these platforms have struggled to leave their controlled laboratory environments and enter the world beyond. While there are a number of reasons for this, perhaps most notably the incredible financial overhead associated with one of these relatively fragile platforms, one major concern in robots is their ability to navigate a world that was not fundamentally designed for them. This extends beyond simple legged locomotion; indeed, the unpredictability of real-world surroundings necessitates use of adaptive strategies to walk on cluttered surfaces, to climb up steps, to crawl to three or four limbs, and to use external supports such as handrails or walls to maintain balance in these complex environs [4].

One of the primary advantages of bipedal platforms is their ability to traverse complex terrains, and the natural extension of this, humanoids with two dedicated manipulators, allows for vastly impressive feats of dexterity. However, in order to perform many of the tasks that humans so thoughtlessly complete daily, it is important that humanoid robots be able to interact with their surroundings beyond a purely locomotory "one foot in front of the other" approach. Though many independent systems will need to be integrated to begin to match the proprioceptive acuity of human beings, proper adaptive strategies for integrating multi-contact scenarios into the robot's controller are necessary to expand the locomotory capabilities of the platform while maintaining the distinct advantages of having versatile limbs not explicitly dedicated to locomotion.

1.3 Multi-Contact Friction Approximation

When extrapolated to the three-dimensional case, many controls procedures can become significantly more complicated. Indeed, since many hand contacts tend to be more for stability than support, only small forces are required at those contact points. Humans use this advantageous force distribution to their advantage, frequently grabbing rails, handles, or

merely placing their hands on flat surfaces and using a combination of normal and tangential forces to generate appropriate stability to the desired locomotory path. However, humans are able to easily detect and mitigate slips of the hands, utilizing the natural tactile abilities of the hands to prevent undesired slippage that could lead to a dangerous fall.

Though there are some existing implementations of tactile sensors used to detect slip (further discussed in Section 2.3), the cognitive ability to measure and accommodate slippery surfaces during operation has been undervalued in humanoid robotics. Especially in non-gravity normal contact scenarios, slip is possible and perhaps even likely if friction considerations are not explicitly made in the whole body controller. Though it is generally sufficient to utilize an extremely conservative estimate of the friction coefficient, this does severely limit the potential applications of force possible at the contact point. It can be difficult to provide accurate information regarding friction before contact due to the relatively small surface properties that most profoundly affect the resulting surface forces, especially in more complex environments where surfaces vary widely and visual systems may not be able to accurately detect minor characteristics. For this reason, it is useful to accurately approximate the friction coefficient of the contact surface before or while loading the contact end effector, and providing compensatory methods in the event of slippage.

1.4 SAFFiR Project Overview

Development of this work is motivated primarily by the U.S. Navy's Office of Naval Research (ONR) Shipboard Autonomous Fire Fighting Robot (SAFFiR) project. The primary goal of SAFFiR is to avoid risking human safety while preventing or suppressing danger aboard a naval vessel. To that end, members of the Virginia Tech Terrestrial Robotics Engineering and Controls Laboratory (TREC) created a humanoid robot capable of performing patrol tasks and addressing potentially hazardous operations. This project resulted in the development of the THOR (Tactical Hazardous Operations Robot) platform.

Following the development of the THOR platform, the TREC lab entered into the competition created by Defense Advanced Research Projects Agency (DARPA). The DARPA Robotics Challenge (DRC) was created to drive academic and corporate teams toward the state of the art humanoid robotics. The challenge was designed to test autonomous robot's ability to navigate a disaster response area and perform manipulation and locomotion tasks

associated with such an unstructured environment. Using the knowledge gained by the development of the THOR humanoid, the Virginia Tech DRC team (Team VALOR) created a new, more capable robotic platform, the Electromechanical Series Compliant Humanoid for Emergency Response (ESCHER) humanoid for use in both the DRC and the SAFFiR project. Among ESCHER's numerous advantages over the previous platform were both the ability to operate on battery power and the addition of two arms adroit mechanical arms provided by HDT Global.

After the DRC was completed in June of 2015, the ESCHER platform was used as the replacement for THOR on the SAFFiR project. Though the platform itself was very capable of collection of tasks that comprised the DRC, it was not ideally suited to the SAFFiR project's interests. This provided the opportunity to improve upon the whole body controller previously implemented, as well as the hardware and software packages available on the robot.

1.5 Thesis Objectives

The objectives of this thesis are as follows:

1. Expansion of ability of ESCHER's whole-body controller to begin approach environmentally constrained locomotion and manipulation tasks.
2. The adaptation of the compliant whole-body control framework to enable multi-contact behavior with the arms of a bipedal platform. This approach is validated through the triped mode of the ESCHER humanoid.
3. Online experimental approximation of static friction coefficient and modification of whole body controller parameters based on the surfaces contacted by the robot's hand.

1.6 Summary of Original Contributions

The contributions of this thesis are the establishment of a base level controls alteration allowing the Virginia Tech humanoids THOR and ESCHER, and any other platform capable of utilizing the ASGARD controls framework, to utilize multi-contact behavior utilizing the joint control state of the manipulation system. These contributions are implemented at

a base level of the control system, as discussed in Section 3.2.3, but implementation is largely focused around the development of the technique for friction coefficient estimation implemented in preparation for the submission of [1]. Additional focus was also placed on attempts to improve capabilities in accordance with our sponsor's, the Office of Navy Research, desire to improve the balance of the ESCHER platform aboard a naval vessel and while completing a number of ship specific tasks, such as walking through a navy door, or bracing in the event of a rocking boat. As such, the primary goals of this project were to establish a base for multi-contact behavior, verify its performance on the robot platform in both simulation and hardware, and establish a feedback control scheme for these interactions without the addition of extraneous hardware or sensor packages.

This involved alteration of the ASGARD framework from the stable bipedal model previously established. Though humanoid platforms would ideally be able to utilize multi-contact control, it is sub-optimal for said platforms to have to always maintain a hand contact; thus it is important to make hand contacts less prioritized in order for normal operation to continue. To this end, the state machines built into the Team VALOR code needed to be altered to allow a multi-contact state with appropriate and safe transitions to provide the ability for the robot's upper level software to initialize said contacts. Transitions to and from this process were developed within the framework of the current state machine in order to provide reliable backwards-compatible performance.

In order to prove the efficacy of this development, a new technique for the experimental acquisition of friction parameters was developed. This method involves the use of no extra sensors to the platform and is capable of approximating the friction parameters between the robot's hand and the contact surface. As mentioned previously, this information allows the expansion or contraction of the support region for the robot, largely based on the gravity-normality of the hand contact surface. With the experimental acquisition of friction parameters, the need to either choose conservative friction values or risk slipping is removed, with an online submodule capable of measuring the static friction and integrating the resulting data into the momentum controller.

1.7 Thesis Outline

The remainder of this thesis separated into 6 chapters, beginning with a review of the literature and underlying concepts applicable to this thesis, before explaining the original contribution of this work and the resulting experimentation derived subsequently. These contents are organized in as follows:

Chapter 2 provides a brief literature review exploring prior works in the development of multi-contact robots, with specific focus on those pertaining to biped systems and friction applications.

Chapter 3 introduces the basic concepts required to understand the ESCHER humanoid, as well as the robot's whole-body controller. It covers the underlying principles design framework of the robot and describes the specifics of the the controller used on the ESCHER platform with a particular focus on the development of a friction-consistent control framework.

Chapter 4 explains the theory behind the multi-contact additions in the ESCHER platform and describes the steps required for the addition of multi-contact capabilities into the platform as well as the necessary considerations for the desired use case. Initial testing and verification of multi-contact functionality is provided.

Chapter 5 presents the results collected from the simulated exploration of the added multi-contact capabilities of the platform. This exploration culminates in development and testing of a novel method for approximating friction on humanoid robots in multi-contact postures. These results evaluate the expansion of the support polygon as well as providing demonstration of added friction estimation capabilities.

Chapter 6 concludes this thesis and presents potential areas for future work and improvement.

Chapter 2

Literature Review

This chapter provides a brief history of bipedal robotics, followed by an overview of momentum control with a focus on multi-contact strategies. The literature review concludes with a discussion of previous implementations of slip detection and response, as well as several other methods of friction coefficient estimation in robotic applications.

2.1 A Brief History of Humanoid Robotics

2.1.1 Bipedal Robot Platforms

After research on several bipedal walking robotic platforms beginning in the late 1960's with the Waseda Legged Platform [5], researchers at Waseda University began development of the biped WABOT 1 [6], the first robot designed to mimic human legs. Though this early design of humanoid robotics was primitive in its implementation, merely replaying pre-planned movement without environmental compliance, it spurred the technology forward, leading to continued the development of the WL and Waseda Biped Humanoid (WABIAN) robot families [5]. During the following decades, humanoid platforms continued to proliferate throughout Japan, leading to the development of such platforms as the Hitachi WH-11 [7], the BLR-G2 [8], and the early implementations that would eventually become Honda's ASIMO Humanoid[9].

As research of bipedal robotics has become more mainstream internationally, there have been

a number of notable humanoid robots throughout the world, some of them even outside of Japan. Boston Dynamics was responsible for bringing in arguably the most popular robot platform of the decade, the Atlas Robot [10], as well as offshoot robot platforms such as PETMAN [11]. Though early versions of the ATLAS were loud and bulky, the new DRC Atlas was developed to be smaller and quieter, using electrical power for hydraulic actuators to provide an extremely capable platform for use indoors and outdoors. Another robot platform, THORMANG [12], developed by ROBOTIS Platforms, was used by numerous teams in the DRC. Other notable humanoid research platforms including the German Aerospace Center's Torque Controlled Humanoid, TORO, [13], the Italian Institute of Technology's WALK-MAN [14], Korea Advanced Institute of Science and Technology's HUBO[15], HRP Series[16], and, of course, Virginia Polytechnic Institute and State University's ESCHER platform.

2.1.2 Development of Bipedal Locomotion

Though early implementations of walking bipeds were able to passively walk via their inherent mechanics or otherwise preprogrammed to perform specific walking actions, control schema quickly demanded a clearer understanding of dynamics of walking in order to establish more versatility. Development of early walking dynamics is largely based upon identification and utilization of the Zero Moment Point (ZMP)[17]. The ZMP has proven to be one of the most constantly relevant and useful metrics of deriving stable walking dynamics. Indeed, it remains significant decades after its inception, providing the backbone for model preview control walking patterns[18], as well as the Generalized ZMP, used in some multi-contact applications[19].

While the ZMP provided a useful framework for bipedal walking generation at Virginia Tech, the introduction of the Capture Point (CP)[20] provided an alternative to ZMP gait generation. The extended version of the CP, the Divergent Component of Motion (DCM) [21], which was further expanded to include the three dimensional case[22], was used as the basis for ESCHER's control scheme. In [23] and [24] Hopkins *et al.* demonstrated the efficacy of the time-varying DCM. This controller utilized time-varying natural frequencies to alter the locomotion algorithm using ZMP reference trajectories.

2.2 Multi-Contact Humanoids

Though utilization of multi-contact locomotion is still a strong distinction between human and robot movement, contact interactions have been studied as far back as the 1980's [25]. Early study of these kinds of interactions was isolated to manipulative applications, largely based on cooperative movement of heavy objects [26], with the parallels between manipulation and locomotion of a floating base not being established until years later.

Though fundamentally the extension of multi-contact control is not strictly different than the rigid body dynamics established for bipedal locomotion, the considerations required for decoupled object behavior and accurate dynamic control of internal forces was not addressed until 1993 with the creation of the virtual linkage model [27]. Research has continued on the virtual linkage model [28], though other methods of force optimization and multi-contact dynamics have been established. The use of the ZMP was expanded to include arm and leg coordination in [19], in order to provide new operational parameters during a multi-contact interaction. The rigid body dynamics in [29], were extended to include task decomposition that included multi-contact support by providing a prioritization of tasks, including posture and support behaviors in a strict hierarchy of performance [30] pertaining to multi-contact support. After initial exploration into multi-contact force distribution [31], applications to other robot platforms works [32, 33], have investigated force optimization and distribution with extension into multi-contact scenarios on actual robots, such as the TORO platform[34], and the Walk-Man robot [35]. Some applications have also considered the distribution of COM force in multi-contact scenarios for both legged robots [36] and bilateral multi-contact applications [37] given friction constraints. Since much of multi-contact scenarios is motivated by a desire for added support points, rather than a necessity for it, recent research in multi-contact applications has focused on hand placement planning strategies [38, 39, 40] focused on when and where to apply hand contacts.

2.3 Friction Approach - Slip Detection and Response

In many floating-base robotic systems, friction coefficients are generally considered values that can be guessed at, with much of the value in their precision being dismissed as unnecessary. However, this floccinaucinihilipilification has not reduced the research into this

area across many other disciplines. In many other scientific areas, knowledge of the active friction coefficients is critical, and, as such, various methods including imaging [41], tactile sensing [42], and micro-vibration detection [43] have all been used to approximate friction coefficients.

Previous research on slip in robots generally focuses on one of three areas: detection, prevention, or recovery. Generally prevention and recovery need to utilize some method of detecting slip in order to appropriately ameliorate the dangers of slip. In most cases, detection is achieved either through use of force and tactile sensors in the feet and ankles, [44, 45, 46, 47]. Alternatively, [48] utilized foot acceleration above a threshold level as detection method for foot slip. Similarly, in [46], Kaneko *et al* created a slip observer to determine when slip had occurred during bipedal walking by balancing measured ankle forces and desired reaction forces. Following this, in [49], this same functionality was used as a method of measuring disturbance forces in their platform HRP-2. Most of these works focus more on slip detection than friction coefficient estimation; however, in [50], Bayrleithner and Komoriya observed that, by analyzing the applied tangential and normal forces in a stick-slip behavior in manipulation, the friction coefficient could be found by finding the peak tangential force before slip occurred, using this value to back calculate the friction force, as is done in this thesis.

Prevention has of slip is generally covered as a hardware implementation, by using higher friction surfaces, like rubber to increase grip contact forces, but some control approaches have been researched. In [51], Kajita *et al.* analyzed the required friction coefficient for an expected motion on a bipedal platform. In order to combat low friction floors, gait pattern generation was then established to eliminate use of high tangential forces on low friction surfaces. Research continued into [52, 53], where knowledge of the friction coefficient was used to generating a purposeful slipping motion in a robot to turn. In contrast to the many detection papers, in [54] Yu *et al.* coordinated the translational and rotational acceleration vectors to reduce the chance of slip. Utilizing the detection of the force balance in the ankles, the biped platform in [47] proposed measuring frictional force directly to establish the value of the static friction coefficient as a method of choosing a gait pattern that wouldn't violate the robot's real friction cone.

Recovery, that the precedes a fall but encourages recalculation of control torques to maintain balance intersects general push recovery strategies [55], but there are some recovery methods focused particularly on slipping. Slipping events were analyzed in [48] and [56], where reflex-

ive response behaviors were used to compensate for the error condition, thus bypassing the need for extensive modeling and calculation within the small recovery time window. More recently [57] established a methodology for slip recovery for a quadruped model using optimized ground reaction forces and analyzing friction parameters during any slip conditions on point feet.

Chapter 3

Overview of Whole Body Control on the Humanoid ESCHER Robot

The purpose of this chapter is to briefly explain the fundamental concepts that underly the following chapters. The following subsections will first provide an overview of the ESCHER robot for which the methods in Chapters 4 and 5 were developed. It will then explain the software hierarchy involved in the operation of ESCHER's operating system, ASGARD, and basic formulations involved in the construction of compliant whole body controllers, with a focus on those aspects that specifically pertain to the Virginia Tech model, the model optimization based on time-varying divergent component of motion.

3.1 Hardware Overview

This section provides an overview of the ESCHER platform with specific focus on its contact points, the feet and manipulators. Additional details are discussed pertaining to the sensor packages onboard through which the robot is able to achieve perception and proprioception.

3.1.1 Anatomy of the Humanoid ESCHER

ESCHER, the Electromechanical Series Compliant Humanoid for Emergency Response, shown in Figure 3.1, is an advanced humanoid research platforms built by the TREC lab

at Virginia Tech for the DARPA Robotics competition in 2015. The robot is currently run on a whole body controller developed by Michael Hopkins [58], modified for this thesis, as discussed later. ESCHER has 38 Degrees of Freedom (DoF), with 6 DoF in each leg, 7 DoF in each arm, and an additional 3 DoF in each hand. The robot stands 1.8 m tall and weighs 77 kg when operating with batteries enclosed in its chest compartment, but only 70 kg when operated with an external power supply.



Figure 3.1: ESCHER platform with 3D printed protective covers. (Photo courtesy of Peter Amico)

3.1.2 Upper Body and Hands

ESCHER's torso is primarily made up of hollow space to allow enclosure of the four lithium polymer batteries used to power the robot when it is untethered from its external power system. There is additional space for the four computers that run the platform: two Gigabyte Brix computers and two ADLQM87PCs, called PC104's. Each Brix contains a quad-core i7 processor operating at 3.2 GHz, and each ADLQM87PC contains a quad-core i7 processor operating at 2.4 GHz. Other miscellaneous circuit boards and electronic hardware are contained in the chest or mounted onboard, including a Nighthawk Router for wireless communication and a Gigabyte network switch for inter-computer communication.

This switch is also tied into the Carnegie Robotics Multisense S7, which is the primary input for visual systems on the platform and includes stereoscopic cameras which can be used for depth sensing, SLAM, and other visual processes. The Multisense is mounted above a rolling Hokuyo UTM-30LX-EWLIDAR LIDAR system, which generates a 3D point cloud of the environment with a higher density and range than the stereo cameras.

ESCHER's HDT Adroit arms each have 7 DoF for movement (shoulder roll pitch and yaw, elbow roll and pitch, and wrist pitch and yaw), with an additional 4 DoF at each hand to allow individual contraction of each of *ESCHER*'s three under-actuated fingers on each hand, as well as an additional DoF for orientation of the thumb with respect to the palm. The arms utilize either position or impedance control, as specified in their startup procedure, allowing potential use of the embedded force-torque sensors in each joint of the arm.

ESCHER's palms are constructed of a rubberized polymer that improves friction parameters between the robot's hand and the object that it intends to manipulate. The palm side of these fingers are each also rubberized, allowing grip of smaller objects, pictured in Figure 3.2b.

3.1.3 Lower Body and Feet

The 6 DoF (separated into hip roll, pitch, and yaw, knee pitch, and ankle roll and pitch) in *ESCHER*'s legs are driven by Maxon BLDC motors integrated with linear Series Electric Actuators (SEA). These SEAs, inspired by the designs of Pratt and Williamson [59], introduce a compliant elastic element between the robot's actuators and the contact load associated

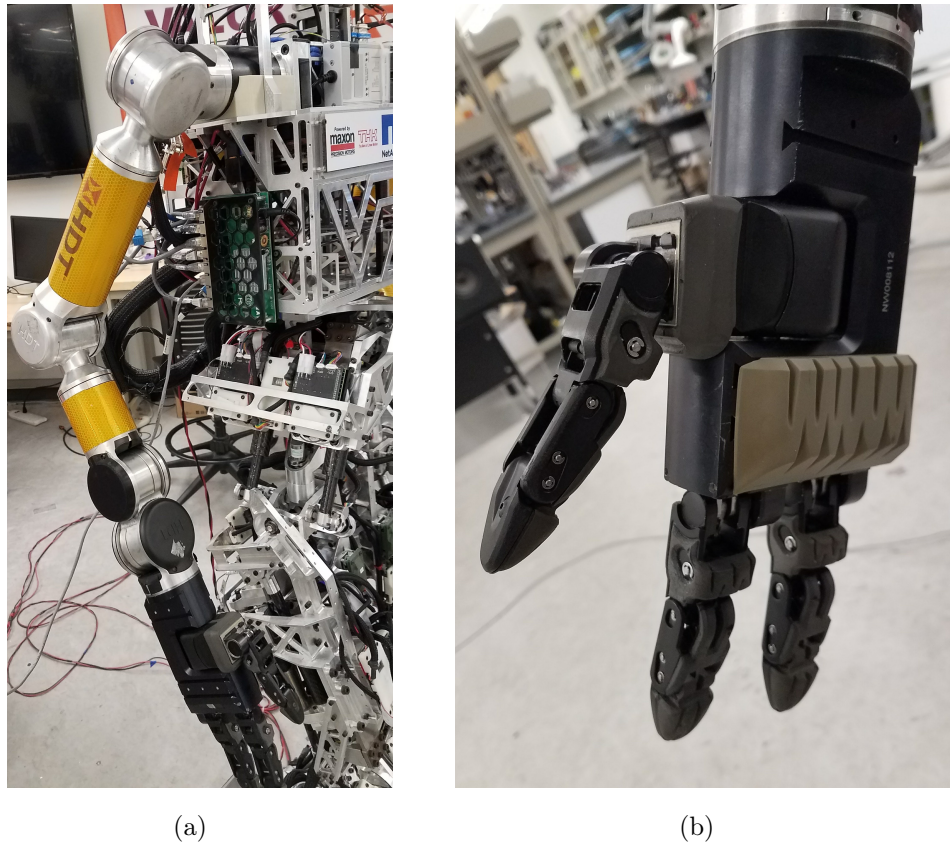


Figure 3.2: An HDT arm is pictured (a) with a closeup of the rubberized palm surface (b)

with its limbs. In doing so, much of the rigidity between the robot and its environment is reduced, allowing for effective force control while eliminating small force responses induced by imprecision.

ESCHER's linear SEAs, as opposed to rotary SEAs, allow for linear actuation, utilizing a cantilevered titanium beam [60] as the compliant elastic link. Not only does this compliance provide a better interface for the force controller to interact with the environment, it is also a practical use of space. Use of the cantilevered SEA allows use of shorter linear actuators, requiring less overall space and allowing a more compact overall design without sacrificing nominal joint torque.

Each actuator in the legs is coupled in series with a Futek LCM-200 tension/compression cell, allowing measurement of the applied tension or compression at each linear actuator. Each joint in the legs is fitted with a Gurley A19 absolute encoder to accurately measure joint position, allowing the robot to know its own body position during locomotion. Additionally,

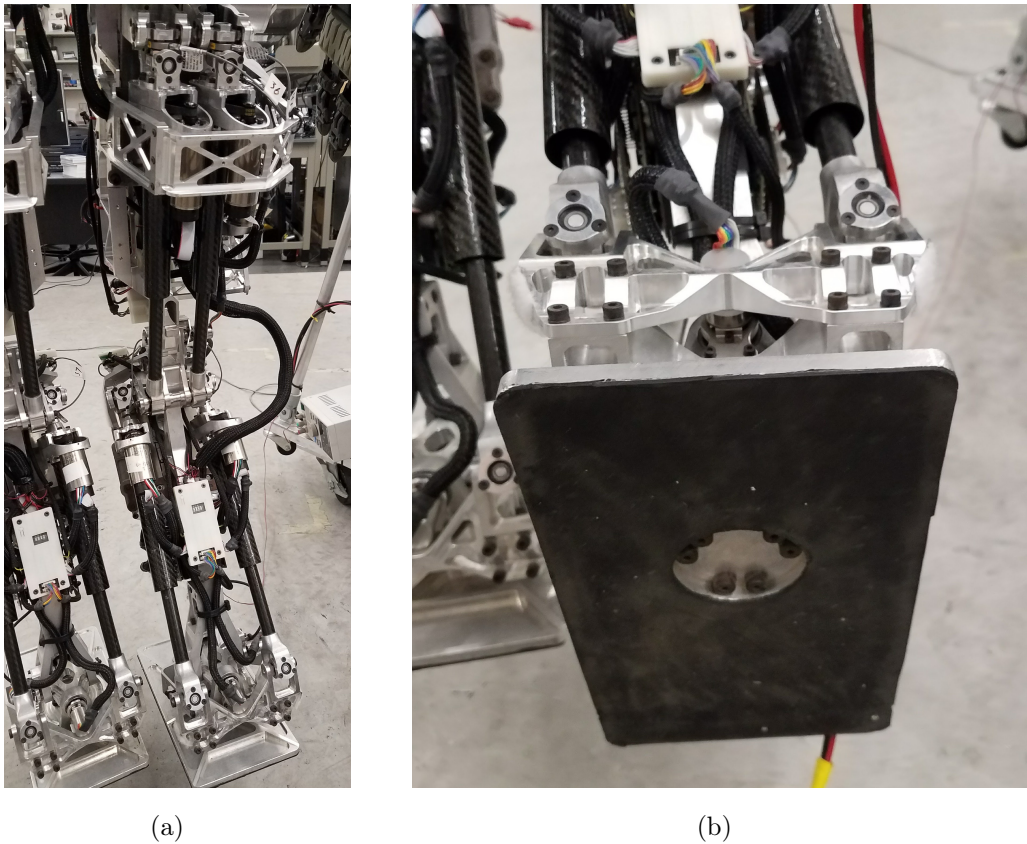


Figure 3.3: *ESCHER*'s right leg is pictured (a) with a closeup of the high friction polymer used on the sole of the right foot (b)

at each ankle an ATIMini-58 six-axis force/torque transducer is mounted to measure the ground reaction force of the feet when touching the ground, information which is input into the momentum controller to determine foot contact status.

ESCHER's feet, as with most of the robot's frame, are constructed out of an aluminum alloy. The bottoms of the feet are covered in a high friction polymer used to increase traction during locomotion. Though slip is not explicitly accounted for in the foot design, it is mitigated largely due to the high friction coefficient between the foot surface and the walking surface. The sole of the foot is pictured in Figure 3.3b.

3.1.4 Additional Sensors

In addition to the Multisense and Hokuyo, the robot has a number of other useful proprioceptive sensors. *ESCHER* was originally constructed with A MicroStrain 3DM-GX3-25 altitude and heading reference system (AHRS) in the pelvis to provide dead reckoning pose estimation to the control system during locomotion. When it was determined that this device alone generated too much noise to properly integrate the desired information during motion, a KVH 1750 Fiber Optic Gyro Inertial Measurement Unit (IMU) was incorporated into the pelvis to mollify this data.

3.2 Software Control Hierarchy

ESCHER's motion system is largely developed around support for the functionality of previous iterations of the platform, most notably the THOR platform. The motion system in its current version is due largely to the work of Michael Hopkins and Robert Griffin who developed the system and its underlying state machines [24]. Due to its early development and ongoing improvements, the Motion System, dubbed ASGARD by the TREC lab, contains ROS (Robot Operating System) support, but does not explicitly use this open source communications framework for its own controls. Since the controls software was developed before ROS interaction was available to the platform, the entire controls software is written in C++ and Lua to operate independently of ROS, with a number of translational layers to allow ROS interaction for useful hardware and software additions.

3.2.1 Motion Manager

The *ESCHER* platform has multiple layers of control, chief of which is the Motion Manager. The Motion Manager is the lowest level software that operated the robot without operating on an embedded device. The Motion Manager serves as the primary interface between external inputs, such as ROS, and the whole body controller. The translational layer, Bifrost, is written to be directly handled by the Motion Manager, and proprioceptive messages from the Communications Manager (Section 3.2.2) are communicated to the rest of the software hierarchy through the Motion Manager module.

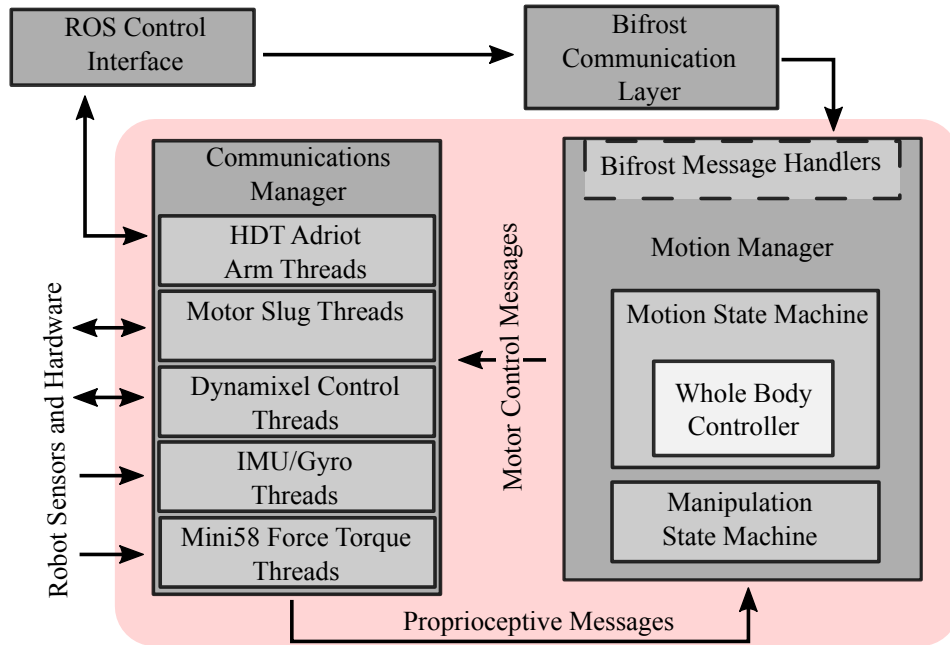


Figure 3.4: The Motion Manager handles the motion control Finite State Machines that house the interface to the whole body controller. Control messages are communicated to the Comms Manager, informed by proprioceptive messages from the instruments.

Motion Manager serves as the home for all of the Finite State Machines (FSMs) that operate *ESCHER*'s functionality. These include the Behavior Machine, the Attention Machine, the Locomotion Machine, and the Manipulation Machine. All of these machines are largely dependent on each other, with the Behavior Machine dictating what modes and transitions are available to the other three, as in Table 3.1.

The Behavior State dictates the performance of the other state machines, allowing fluid control between operational goals. While there are a number of useful states during operation. The robot generally operates in some variation of the Stand state, using this to transition to states like Manipulation or Multi-Contact as needed to establish those operations. This is useful to ensure that each of these more complex states is begun from a stable stance before performing the desired task.

The Locomotion State is most important to *ESCHER*'s operation; it is the state machine that determines the operation of the whole body controller, whether the robot is walking or standing. The locomotion state has modes for particular manipulation states, which allows it to balance when manipulation is utilized, or alternately allows control of the robots

Table 3.1: Mapping of the Behavior and Motion States in the ASGARD Motion System

Behavior	Motion System State Machines		
	Locomotion	Manipulation	Attention
Fall	Fall	Slave	Slave
Freeze	Ready	Slave	Slave
Freeze Manipulate	Ready	Joint Teleop	Look
Get Up	Get Up	Slave	Slave
Idle	Idle	Slave	Slave
Multi-Contact	Multi-Contact	Multi-Contact	Look
Soft Stop	Stand	Joint Teleop	Look
Stand	Stand	Slave	Look
Stand Cartesian Teleop	Stand	Cartesian Teleop	Look
Stand Manipulate	Stand	Joint Teleop	Look
Stand Prep	Prep	Slave	Slave
Step	Step	Slave	Look
Step Manipulate	Step	Joint Teleop	Look
Walk	Walk	Slave	Look
Walk Manipulate	Walk	Joint Teleop	Look

arms when manipulation and multi-contact goals are not being pursued. The Manipulation State dictates how much the arms are used for balancing, whether they are enslaved by the Momentum Controller or able to be teleoperated by *ESCHER*'s operator. As discussed later, the addition of a Multi-Contact state allows one arm to be used as a support point while the other remains teleoperable. The Attention State is responsible for movement of the head allowing several modes. Though the Attention State is generally left as a teleoperable state for the user to utilize for manipulation and navigation tasks, it also has modes for tracking objects and scanning for targets.

3.2.2 Communications Manager

The Communications Manager acts as the primary interface between *ESCHER*'s many sensors to the rest of the operation system. The Communications Manager varies robot to robot due to the use of different sensors on each platform. However, in each it serves as the hub of sensor data, collecting force-torque information, joint tensions and positions, as well as the gyroscopic data from the onboard IMU.

This information is communicated to the Motion Manager for use on the whole body controller and for transfer to the Bifrost communication layer for other packages to utilize. The sole divergence from this is the use of the HDT arms, which are run directly by ROS messages from their own ROS packages. As a result, these arms send and receive data through direct ROS interaction, but their controller interface to the Motion System is still housed in the Communications Manager, Figure 3.4.

3.2.3 Momentum Controller

The Momentum Controller on *ESCHER* was initially developed by Michael Hopkins to provide robust balancing and locomotion through time-varying DCM control as described in [58]. This controller utilizes the time-varying Divergent Component of Motion to ensure balance using the two feet. By generating a desired DCM trajectory and then solving for a set of achievable joint torques to minimize DCM tracking error on that trajectory, the controller can set the robot into motion in a particular direction at a particular speed. Since the HDT arms are run on position control, as is the rolling LIDAR on *ESCHER*'s head, these joint trajectories are integrated into position and velocities to allow control of all joints in the robot. Further discussion of this control is discussed in 3.3 and both the theory and programming expanding use of the controller are discussed in Chapter 4. Though whole body control can be described as a subsystem of the Motion Manager, it is ultimately the core of the robot's locomotion and is intrinsically tied to the *ESCHER*'s operation, working largely in series with the other elements of the Motion System, rather than as a subsystem of any other piece.

3.3 Optimization Based Whole Body Control

3.3.1 ESCHER's Rigid Body Dynamics

Control of an actuated humanoid with n degrees of freedom (DoF) can be described by the vector \mathbf{q} , where $\mathbf{q} = \begin{bmatrix} \mathbf{q}_0^T & \dots & \mathbf{q}_n^T \end{bmatrix}^T \in \mathbb{R}^{6+n}$ such that $\mathbf{q}_0 \in \mathbb{R}^6$ represents the location and orientation of the floating base and $\mathbf{q}_n \in \mathbb{R}^n$ is the vector of robot joint positions. Based on this, the floating-base rigid body equation to describe ESCHER's dynamics is given as

$$\begin{bmatrix} 0 \\ \boldsymbol{\tau} \end{bmatrix} = \mathbf{H}(\mathbf{q})\ddot{\mathbf{q}} + \mathbf{C}(\mathbf{q}, \dot{\mathbf{q}}) - \sum \mathbf{J}_c^T \begin{bmatrix} \mathbf{f}_{\text{foot},l} \\ \mathbf{f}_{\text{foot},r} \end{bmatrix}, \quad (3.1)$$

where $\boldsymbol{\tau} \in \mathbb{R}^n$ is the vector of joint torques, \mathbf{H} is the joint-space inertia matrix, and \mathbf{C} is the vector of centrifugal, Coriolis, and gravity torques, and $\mathbf{f}_{\text{foot},l}$ and $\mathbf{f}_{\text{foot},r}$ are representative of the robot's contact forces at each of its feet with corresponding foot Jacobian matrix, \mathbf{J}_c .

3.3.2 Time-Varying Divergent Component of Motion

From [22], the Divergent Component of Motion is defined as

$$\boldsymbol{\xi} = \mathbf{x}_{\text{com}} + \frac{1}{\omega_0} \dot{\mathbf{x}}_{\text{com}}, \quad (3.2)$$

where \mathbf{x}_{com} and $\dot{\mathbf{x}}_{\text{com}}$ are the position and velocity of the center of mass, respectively, and $\omega_0 = \sqrt{\frac{g}{\Delta z_{\text{com}}}}$ is the natural frequency of the linear inverted pendulum [61] given a nominal CoM height, Δz_{com} . As adapted in [23], the time-varying Divergent Component of Motion is defined as

$$\boldsymbol{\xi} = \mathbf{x}_{\text{com}} + \frac{1}{\omega(t)} \dot{\mathbf{x}}_{\text{com}}, \quad (3.3)$$

and $\omega(t) > 0$ is the time-varying natural frequency of the DCM. By moving this point, the controller can move the platform's center of mass to follow an instructed trajectory, allowing the robot to walk and shift its weight to balance.

The DCM is moved by controlling the virtual repellent point, first introduced in [22], which

serves as the unstable equilibrium point of the robot's DCM dynamics.

$$\mathbf{r}_{\text{vrp}} = \mathbf{x}_{\text{com}} - \frac{\dot{\mathbf{i}}}{m(\omega^2 - \dot{\omega})}, \quad (3.4)$$

where $\dot{\mathbf{i}} \in \mathbb{R}^3$ is the linear momentum rate of change, and m is the system mass. The DCM is repelled by the VRP at a rate proportional to its distance, allowing movement of the DCM by external VRP control. Using this point, the first order dynamics of the DCM become

$$\dot{\boldsymbol{\xi}} = \left(\omega - \frac{\dot{\omega}}{\omega} \right) (\boldsymbol{\xi} - \mathbf{r}_{\text{vrp}}), \quad (3.5)$$

This system is unstable with respect to the VRP when $\omega - \frac{\dot{\omega}}{\omega} > 0$. However, like its time-invariant counterpart, the CoM dynamics can be stabilized by tracking a desired DCM reference trajectory with control based on the VRP [24].

These points provide the basis for generating three-dimensional trajectories to control the balance and motion of the platform during operation. By manipulating the VRP, the DCM can be moved around inside, or indeed outside, the support polygon to create movement in the robot's center of mass.

3.3.3 Task Space Formulation

For an arbitrary point on the robot associated with some task t , the acceleration of said point may then be expressed

$$\ddot{\mathbf{x}}_c = \dot{\mathbf{J}}_t \dot{\mathbf{q}} + \mathbf{J}_t \ddot{\mathbf{q}}, \quad (3.6)$$

where $\ddot{\mathbf{x}}_c$ refers to the acceleration of the contact point, and $\dot{\mathbf{J}}_t$. The rigid body dynamics presented in Equation 3.1 are predicated on a number of assumptions; paramount amongst these is that no slip occurs at the contact locations. This assumption is largely fulfilled by either knowledge or conservative estimates of the available friction parameters and their effect on the platform. The no-slip condition is generally fulfilled by constraining $\ddot{\mathbf{x}}_c = 0$. This assumption aligns with Coulomb friction by keeping the applied forces at \mathbf{x}_c within the corresponding friction cone, as in Figure 3.5.

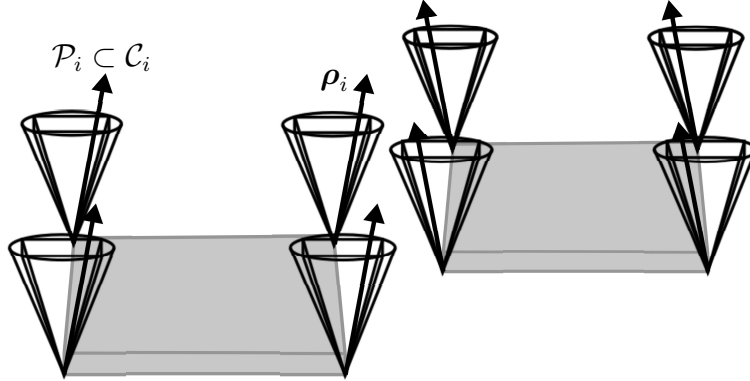


Figure 3.5: Friction pyramids, \mathcal{P}_i , are inscribed in friction cones, \mathcal{C}_i , at the bounding corners of each foot. The generalized forces ρ_i operate within these pyramids to avoid friction limits

The frictional constraints on the contact forces can be described using a convex second order cone constraint,

$$f_{c,x}^2 + f_{c,y}^2 < (\mu_s f_{c,z})^2, \quad (3.7)$$

as shown with the friction cones in Figure 3.5. However, utilizing exclusively Equation 3.7 requires the addition of a quadratic constraint to the model optimization, significantly increasing the complexity of solution. To address this, the friction cone can instead be conservatively described with an inscribed pyramid \mathcal{P}_i , comprised of m basis vectors $\mathbf{B}_{c,m}$ [62, 63],

$$\mathbf{f}_c = \sum_m \mathbf{B}_{c,m} \rho_{c,m}, \quad (3.8)$$

where $\rho_{c,m}$ is the generalized contact force along vector m at contact point c . This has the advantage of reducing the frictional constraint to the linear domain, enabling much faster solution approaches. This constraint then ensures that the force \mathbf{f}_c always lies within the friction cone.

3.3.4 Model Based Optimization based on Time-Varying DCM

The goal trajectory for the CoM can then be solved for using the robot's inverse kinematics and the rigid body dynamics (Equation 3.1) to calculate the set of joint torques that

minimize the tracking error of each operational goal, such as momentum rate of change or frictional contact limits, while satisfying the dynamic constraints of the system. To do this, ESCHER's whole body controller utilizes a linearly constrained quadratic program (QP) solver to optimize joint accelerations and contact forces

$$\min_{\ddot{\mathbf{q}}, \boldsymbol{\rho}} \|\mathbf{C}_b(\mathbf{b} - \mathbf{J}\dot{\mathbf{q}} - \mathbf{J}\ddot{\mathbf{q}})\|^2 + \lambda_{\ddot{\mathbf{q}}}\|\ddot{\mathbf{q}}\|^2 + \lambda_{\boldsymbol{\rho}}\left\| \begin{bmatrix} \boldsymbol{\rho}_{\text{feet}} \\ \boldsymbol{\rho}_{\text{hands}} \end{bmatrix} \right\|^2, \quad (3.9)$$

such that:

$$\mathbf{A}\dot{\mathbf{q}} + \mathbf{A}\ddot{\mathbf{q}} = \sum_c \mathbf{W}_c \begin{bmatrix} \mathbf{f}_{\text{foot},l} \\ \mathbf{f}_{\text{foot},r} \end{bmatrix} + \mathbf{w}_g \quad (3.10)$$

$$\underline{\mathbf{q}} \leq \mathbf{q} + T\dot{\mathbf{q}} + \frac{1}{2}T^2\ddot{\mathbf{q}} \leq \bar{\mathbf{q}} \quad (3.11)$$

$$\underline{\boldsymbol{\tau}} \leq \boldsymbol{\tau} \leq \bar{\boldsymbol{\tau}} \quad (3.12)$$

$$0 \leq \boldsymbol{\rho}_{\text{feet}}, \quad (3.13)$$

where \mathbf{C}_b is representative of the task weighting matrix such that $\mathbf{Q}_b = \mathbf{C}_b^T \mathbf{C}_b$ is the semi-positive definite weight matrix, \mathbf{b} is the vector of desired motion tasks, \mathbf{J} is set of stacked Jacobians, $\lambda_{\ddot{\mathbf{q}}}$ and $\lambda_{\boldsymbol{\rho}}$ are regularization parameters, and c denotes contact. The weighting matrix allows soft prioritization of motion tasks, as opposed to the strict prioritization in [64, 65], with high weights associated with stationary contact points, and low weights are often assigned to angular momentum rate of change to improve dynamic stability. \mathbf{A} is the centroidal momentum matrix [66], $\mathbf{W}_c \in \mathbb{R}^{6 \times 3}$ maps contact forces to wrenches acting about the CoM, and $\mathbf{w}_g = [0, 0, mg, 0, 0, 0]^T$ encodes the force of gravity \mathbf{w}_g . The constraints in Equations 3.10, 3.11, 3.12, and 3.13 ensure that the achieved values are within specified joint and torque limits, and ensure the dynamic equality and unilaterality of the solution's force balance. This implementation of the whole body controller allows the variation of desired forces at contact points to provide a basis for generating a set of joint torques to achieve a desired CoM position through DCM control.

Chapter 4

Multi-Contact Momentum Control on the ESCHER Humanoid

The ESCHER platform has always had control of both arms and legs, but was not explicitly constructed with purpose of being able to institute multi-contact operation. This is demonstrable in both the software and hardware, as the development of the Momentum Controller utilizes only the contact forces associated with the feet. To address this consideration and others, the robot’s software architecture needed to be modified on several levels to allow multi-contact control of the robot. These modifications and the design considerations that influenced their development are discussed below.

4.1 Multi-Contact Design Goals

The whole body controller implemented in [58] has proven robust enough to provide the basic operation of ESCHER’s walking process, even utilized in applications with stairs or uneven ground; however, it does have some shortcomings. Most notably in this instance, is the lack of integrated multi-contact support. As shown in Equations 3.1 and 3.9, the contacts used as input and output forces to the system are all based around the feet. Since the whole body controller is not otherwise agnostic, this means that forces applied to other locations, such as the hands, are not treated as controllable inputs, but instead as unpredictable disturbances. The practical upshot of this is that, while the platform is kinematically capable of reaching

out to steady itself with a hand, the whole body controller does not actively utilize this potential stabilizing method, even when it might prove advantageous.

While developing a methodology to add multi-contact implementation to the robot’s whole body controller, a number of considerations needed to be addressed. First, for both backwards and forwards compatibility, it was necessary that any modifications be within the current framework, adopting the time-varying DCM momentum controller from [58], and working within the limitations of the available hardware on both the *ESCHER* and *THOR* platforms. This meant that use of additional sensors was, while plausible, to be avoided. Additionally, for performance and compatibility, software modifications should be within the Lua/C++ *ASGARD* framework, both for simplicity and extensibility.

Additional considerations were made to avoid violation of the soft-prioritization strategy previously applied to *ESCHER*’s control optimization. By following the current implementation of the controller, Equation 3.9, and its constraints, the robot would be able to utilize the hands for balance as much or as little as needed based on the weight parameters provided to the relevant joint accelerations.

Finally, the application was placed within context of the real world, primarily pertaining to its funded purpose with the ONR, patrol and monitoring of a naval vessel. In this circumstance, the robot should be able to operate relatively safely and robustly around humans, avoiding dangerous movement and providing maximum support to avoid significant failures. This involved keeping movement within safe torque and velocity limits, as well as keeping new behaviors, like multi-contact balancing, from interfering with the walking and manipulation behaviors already on board. This included developing a directional methodology for transitioning between the locomotion, manipulation, and behavioral states on the robot that limit instability while still providing the full suite of operational behaviors in *ASGARD*.

4.2 Modification of *ESCHER*’s Momentum Controller

4.2.1 Updating the Rigid Body Dynamics

In accordance with Equation 3.1, the torque-controlled humanoid is moved by the aggregate of its internal and external forces, so accurate knowledge of the model’s inertia, as well as its various positions and velocities, is key to the proper joint torque calculations. Since all of

these values are used by the robot independent of the number and type of contacts applied, no modifications need be made to the inertial, gravity, or Coriolis parameters.

Utilizing the vector \mathbf{q} from Section 3.3.1, where $\mathbf{q} = [\mathbf{q}_0^T \ \dots \ \mathbf{q}_n^T]^T \in \mathbb{R}^{6+n}$ provides the current state of the robot, the rigid body dynamics presented in Equation 3.1 can be adapted to include hand contacts relatively simply, such that

$$\begin{bmatrix} 0 \\ \boldsymbol{\tau} \end{bmatrix} = \mathbf{H}(\mathbf{q})\ddot{\mathbf{q}} + \mathbf{C}(\mathbf{q}, \dot{\mathbf{q}}) - \sum \mathbf{J}_c^T \mathbf{f}_c, \quad (4.1)$$

where \mathbf{f}_c is an expansion of it's previous value to become

$$\mathbf{f}_c = \begin{bmatrix} \mathbf{f}_{\text{foot},l}^T \\ \mathbf{f}_{\text{foot},r}^T \\ \mathbf{f}_{\text{hand},l}^T \\ \mathbf{f}_{\text{hand},r}^T \end{bmatrix}. \quad (4.2)$$

The first step in integrating the use of hand contacts is to modify the \mathbf{J}_c and contact force terms. The with the addition of two potential contacts, the size of \mathbf{f}_c doubles, allowing contact wrenches not only for the feet but also for the hands. There is a similar expansion of the Jacobian matrix \mathbf{J}_c with the addition of the calculated Jacobians relating the hand end effector velocities to the center of mass velocities, much as the rest of the \mathbf{J}_c term is a relation of the foot velocities to the center of mass velocities.

4.2.2 Task Space Formulation

Though friction cones are the most accurate representation of the available range of motion for a contact point, assuming unilaterality, [62] demonstrated that it is possible to simplify these cones to polygons, in our case pyramids. This adjustment allows faster solution of the optimization problem through linearity. To that end, new contact points and their associated contact forces, described as $\boldsymbol{\rho}_i$, where i indicates the corner of each end effector, are added to the the $\boldsymbol{\rho}$ vector in Equation 3.9. These $\boldsymbol{\rho}$ values are mapped to the length and width of the approximated contact surface for task space formulation, Equation 3.8, and are used as a distributed representation of the point wrench applied by the end effector.

To accommodate the addition of the hands ot this parameter, 8 new values $\boldsymbol{\rho}_i$ values are

added to the $\boldsymbol{\rho}$ matrix. With this adaptation the hands and feet both are utilized in the optimization of forces.

4.2.3 Expanded Model Optimization

With the rigid body dynamics properly adapted, the optimization (Equation 3.9) is updated to include the use of the two additional contact points through the $\boldsymbol{\rho}$. Though basic operation of the weighting parameters associated with the momentum controller's operation do not need to be changed, the weights associated with a multi-contact orientation are modified to high values, as opposed to the relatively low values they hold in less hand-prioritized operation. This mechanism allows the platform to prioritize maintenance of hand location when in contact with a surface, but, due to the more forgiving soft prioritization of weighting, not do this at the expense of balance or posture.

As for the constraints associated with the optimization, no major overhaul is required, as torque and joint limits are based on the performance of the hardware itself, which has not changed. However, Equation 3.10 is modified to accommodate the input from the forces of the hands

$$\dot{\mathbf{A}}\dot{\mathbf{q}} + \mathbf{A}\ddot{\mathbf{q}} = \sum_c \mathbf{W}_c \begin{bmatrix} \mathbf{f}_{\text{foot},l} \\ \mathbf{f}_{\text{foot},r} \\ \mathbf{f}_{\text{hand},l} \\ \mathbf{f}_{\text{hand},r} \end{bmatrix} + \mathbf{w}_g, \quad (4.3)$$

where the contact force matrix is increased and \mathbf{W}_c is expanded to include the mappings of contact wrenches for the hands to the CoM. Additionally, Equation 3.13 adds use of the hands to its unilaterality constraint,

$$0 \leq \boldsymbol{\rho}. \quad (4.4)$$

It is worth noting here that, while not actively implemented here, unilaterality in the hands is not explicit. Unlike the feet, which are generally used exclusively for pushing in humanoids, hands can and often do function bilaterally to push and pull in a grip. That behavior, though

significantly more complicated, would not require constraints on the minimum value of $\boldsymbol{\rho}$, as negative values, i.e. pulling, would be achievable.

4.3 Software Implementation

4.3.1 Adaptation of the Momentum Controller Subclass

The programmatic equivalent of Section 4.2 occurs largely in the `MomentumController` subclass in the *ASGARD* framework. Though there are several wrapper classes associated with this class, to convert sensor data from throughout the robot to the communications and motion managers, most of the more intricate modifications are housed in this subclass.

The rigid body dynamics are expanded to utilize forces at the hands and their corresponding Jacobians. This is relatively simple in *ESCHER*'s momentum controller, since calculations of the Jacobians are handled by the model knowledge of the platform and by a Jacobian Lua class.

In *ESCHER*'s Momentum Controller, the optimization is solved using the `quadprog` wrapped C++ object, specifying that

$$\min_{\ddot{\mathbf{q}}} \frac{1}{2} \ddot{\mathbf{q}}^T \mathbf{G} \ddot{\mathbf{q}} + \mathbf{g}_0^T \ddot{\mathbf{q}} \text{ such that } \begin{cases} A \cdot \ddot{\mathbf{q}} \leq b, \\ A_{eq} \cdot \ddot{\mathbf{q}} = b_{eq}, \end{cases}, \quad (4.5)$$

where \mathbf{G} and \mathbf{g}_0 are matrices of the associated joint acceleration and contact force costs, b specifies the inequality constraints represented by max wrench and torque limits for each of the contact points and joints respectively, as well as the unilaterality constraint of contact, and A specifies the robot's inertial state. Similarly, b_{eq} represents the linear constraints for the optimization such that the applied $\boldsymbol{\rho}$ values are within the specified friction cones, and the net wrenches applied are equal to the system forces from gravity, etc.

This solver allows enforcing of the necessary optimization constraints, Equations 4.3, 3.11, 3.12, and 4.4 through its equality and inequality constraints. This is done with the specification of minimum and maximum limits on the total wrench of the robot that may be applied to the hands as well as maintaining force application within the specified friction cone, delineated by use of a four separate μ values, one for each of the hands and one for each

of the feet. These are set as optimization constraints, b , keeping the robot from exceeding the maximum joint torques possible for the motors to achieve, as well as preventing slip on contact surface. However, without any accurate knowledge of the friction coefficients of the contact points, the optimized solutions do not guarantee a no-slip condition, which is one of the primary assumptions of the rigid body dynamics model. The centroidal dynamics, Equation 4.3, are fulfilled with the equality constraint, b_{eq} .

With the calculated joint accelerations from the optimization equation, the robot is able to apply forces with each of its in-contact end effectors, which are designated via a selection matrix applied to \mathbf{G} and \mathbf{g}_0 above. With the knowledge of $\ddot{\mathbf{q}}$, the corresponding joint torques, $\boldsymbol{\tau}$, can be calculated to control the robot. The desired forces are extrapolated from the minimized $\boldsymbol{\rho}$ from Equation 3.9 and can be mapped to the single point wrench to determine net force application at the contact point, $\mathbf{f}_{\text{hand},l}$ for example, in accordance with the model established in Section 4.2.

4.3.2 Additional Machine States

With the Momentum Controller properly adapted to allow multi-contact control, adjustments were made to the *ESCHER* controller. This consists of two state machines, one for the robot’s overall movement state, the Locomotion State Machine, and one for the robot’s overall manipulation state, the Manipulation State Machine.

To allow multi-contact support, an adaptation of the robot’s stand state was developed for the locomotion state. On user input, the robot is able to transition into and out of the multi-contact state from the stand-manipulate state. This state class serves as a master of the necessary operations for maintaining balance and establishing multi-contact control. It fetches sensor readings from the communications manager and uses them to calculate the DCM trajectory which is then compared to the current robot state to check for a fall case. It also serves as the interface for exiting and entering the multi-contact state during regular operation.

Without any onboard sensors to indicate necessity for such a multi-contact transition, such a transition is currently only triggered manually. With the hand approximately in contact with the support surface, the robot may be told that a contact has been established. When this signal is received, the whole body controller selection matrix accepts hand contacts as a

method of force output and allows the robot to utilize its hand contacts accordingly. These contacts are slowly loaded, limited by the applicable velocity and torque limits on the arms in the whole body controller. When the robot is triggered to exit the multi-contact state, the exit functionality is called in the `locomotion_multi_contact` state, making it possible to deload the hand and return to the `stand_manipulate` state, in which the hand placement is maintained, but balance management is provided exclusively by the foot contacts.

To address some of the operational and safety concerns outlined in section 4.1, the multi-contact state was implemented with two additional features. The first, and arguably more useful, is a desired contact force input for each hand. Using the mapped force limits from the momentum controller, this functionality allows application of a specific amount of force to be a parameter to the whole body controller with a relatively high desired weight. Using this, the controller will attempt to come as close as is reasonably possible to using the desired force at the preferred contact, allowing distribution of forces should the robot need to utilize its hand force at a particular magnitude. The second functionality serves as a safeguard against slipping and related unexpected behaviors. Since *ESCHER* and *THOR* both lack contact sensors on their palms, it is possible that an operator might inform the robot of hand contact when none has been achieved. This behavior would result in the robot blindly attempting to put weight onto a hand hanging in mid air, an unbalanced behavior that could lead to a fall. To prevent this, a switchable slip detection technique is implemented in the `locomotion_multi_contact` state. It uses the hand calculated velocity, based on the sensor values of the body and arms, as a slip detector. When the velocity is above some threshold value, for this implementation 0.1 m/s, it is assumed that the contact point either does not exist, or is unstable, in which case the robot ceases multi-contact on that hand and returns to a no-contact orientation to stay balanced.

In order for the robot to successfully move its arms and maintain a contact point during the multi-contact state, an additional manipulation state was developed. This manipulation state serves largely to compliment the locomotion state, operating largely as a container of the appropriate weighting parameters for multi-contact and manipulation for the platform. When a hand is placed in contact with a support surface, the `manipulation_multi_contact` state increases the acceleration weight associated with that contact point, making maintenance of that contact location a greater priority to the whole body controller, penalizing actions that require severing that contact point. When the hand is removed, weighting parameters are reduced, allowing the whole body controller to utilize the arm's movement more

effectively for standard double support balancing.

4.4 Resulting Operation

Qualitative operation of this multi-contact poses can be seen in Figure 4.3. The robot approaches a box, extends a hand via preprogrammed teleoperation (4.3b), and lowers it to the box's surface to transition from `stand_manipulate` to `multi_contact` is made (4.3c). When instructed, the CoM position is moved 0.3 m forward in the x direction, allowing further distribution of force onto the hand contact (4.3d).

Additional operational features as discussed in Section 4.3.2 can be seen in Figure 4.4. The robot is actively utilizing the box to support a small portion of its weight (10 N). When the support surface is suddenly removed, the robot's balance begins to slip as the it attempts to apply a force to a contact point that is no longer achievable. However, once the threshold hand velocity value has been reached, the system is able to recover, removing the applied hand force from the whole body controller and resulting to a purely bipedal support mode.

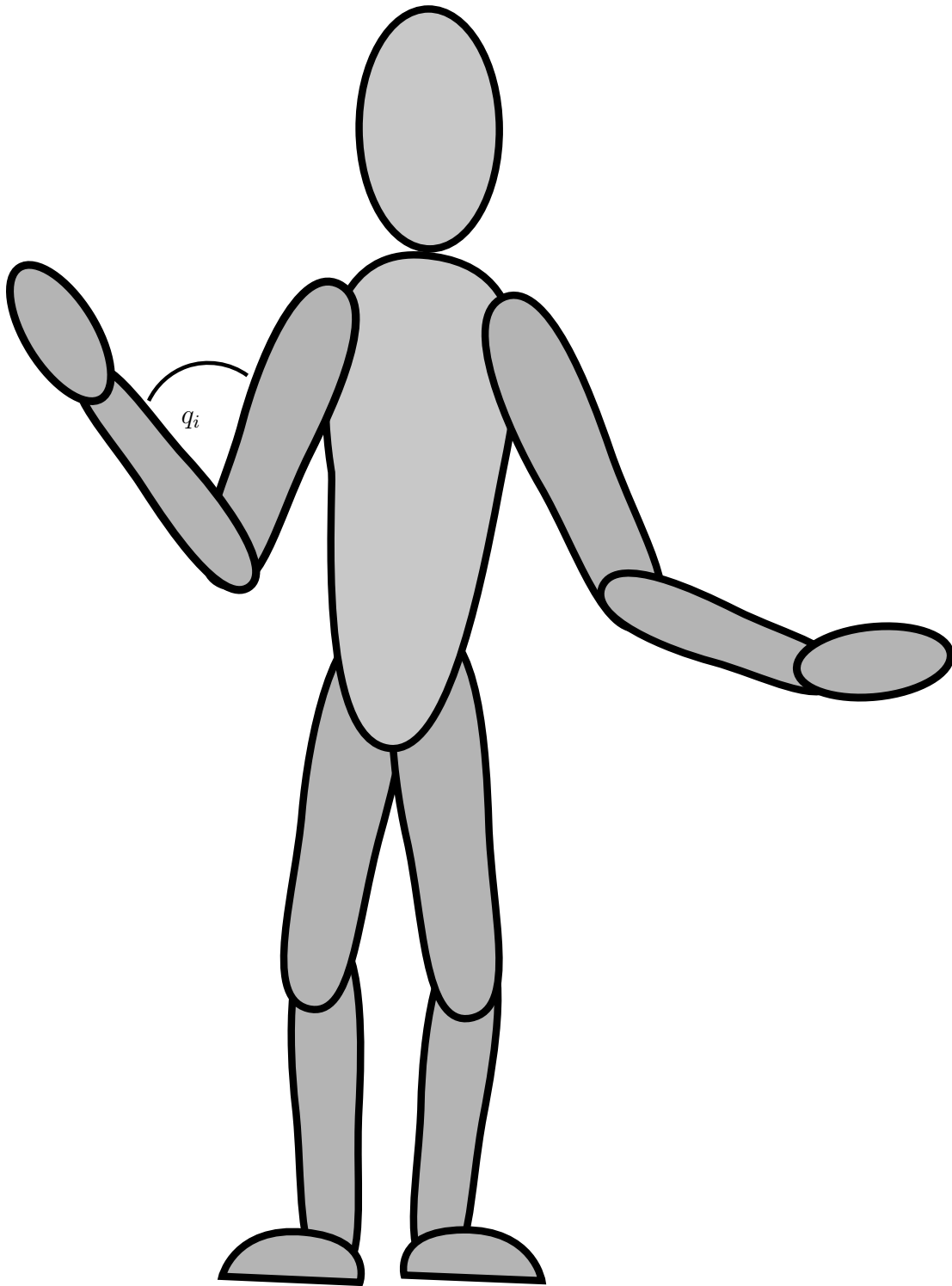


Figure 4.1: Friction cone and friction pyramid distributed representations of localized end effector contact points on palm (left) and foot (right) [1]

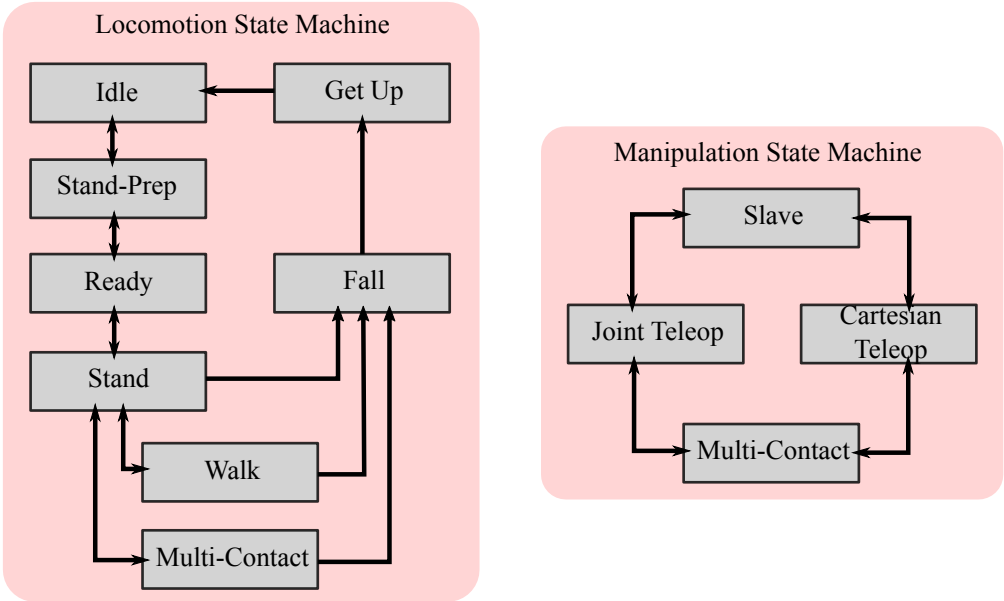


Figure 4.2: The state machine dictates operational parameters and admissible inputs for the robot at any given time. This allows a safe transition to and from the multi-contact states by having them travel through the `locomotion_stand_manipulate` state

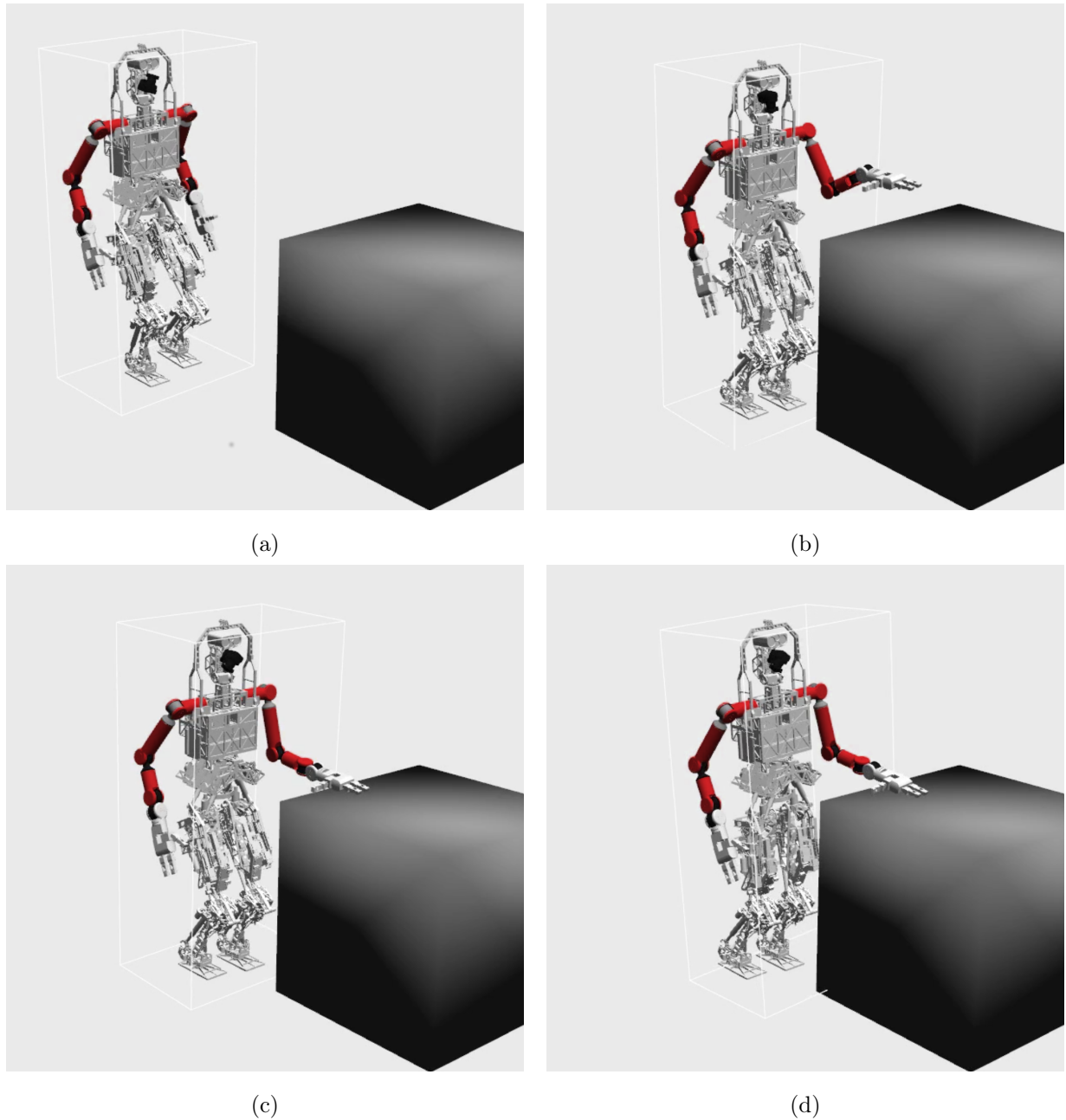
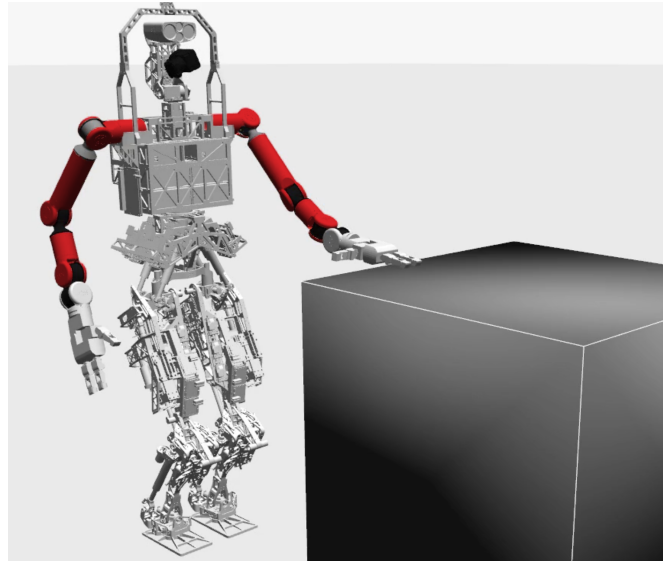
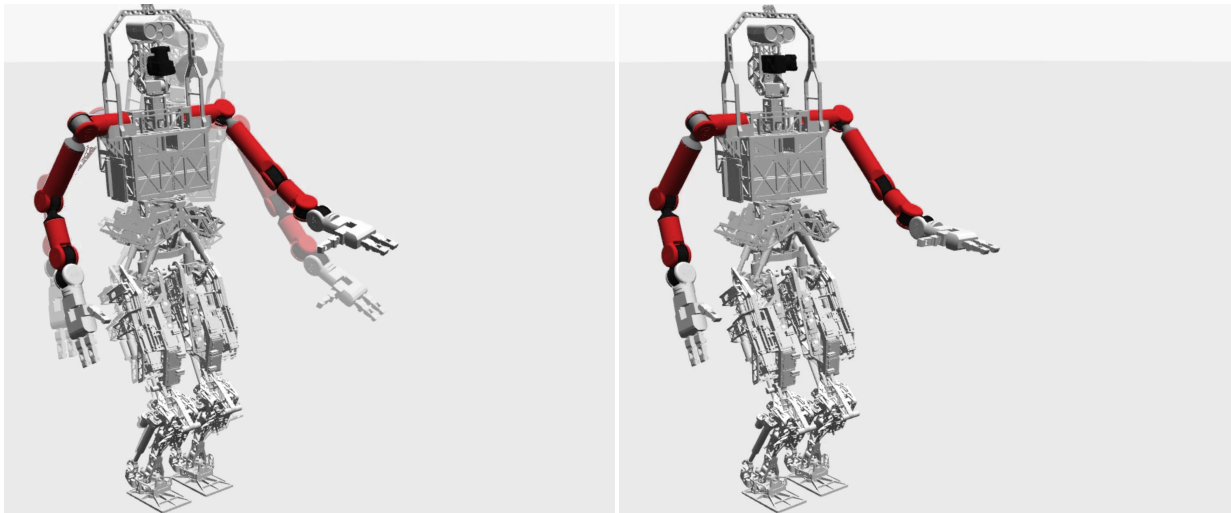


Figure 4.3: *ESCHER* approaches the box (a), extends a hand and initiates contact via preprogrammed teleoperation (b-c). With multi-contact functionality enabled, the robot is able to shift its center of mass closer to the platform and utilize its new contact point for stability (d).



(a)



(b)

(c)

Figure 4.4: The robot begins in a multi-contact pose (a). When the support is suddenly removed, the weight being placed on the robot causes a brief downward lurch (b), before slip is detected. Once slip is detected, the robot reorients to a balanced pose without multi-contact (c)

Chapter 5

Online Multi-Contact Friction Estimation - A Case Study

To establish the usefulness of the multi-contact whole body control model, the expanded controller developed in Chapter 4 is utilized as a base for creating a friction measurement technique for humanoid robots with ankle-mounted force torque sensors. This technique is described below after a brief discussion of the importance of accurate friction parameters. This added functionality is developed based first on Coulomb's Law of Friction as well as disturbance force detection using ankle mounted force torque sensors. After describing these aspects of the formulation, a simple simulation demonstrating the proposed technique is shown, followed by application on both the simulated and physical ESCHER platforms. This chapter concludes with a discussion of the proposed technique's results and its overall efficacy.

5.1 Significance of Friction Parameters

In general, slipping in bipeds is a niche research area, largely for the same reason that humans are not largely concerned with slipping on a day-to-day basis. Though people do slip while walking, it is relatively rare occurrence, usually avoidable by preparing for a potentially slippery environment with the proper equipment, like climbing or snow shoes, or by avoiding a recognized slippery area, like giving a wide berth to a "Caution: Floor Slippery when

Wet" sign. However, in the instances in which humans are required to traverse a potentially slippery surface, there is usually an almost unconscious "testing of the waters", as it were. This is easily exemplified watching a first-time ice-skater enter a ice rink. This human might place one foot out on the ice, and push lightly against it, approaching at a perpendicular angle and pushing out against the surface of the ground. In this action, this skater is delicately testing the friction of the surface, establishing how likely he is to slip on his next step out onto the ice.

A similar technique to this has been employed in [47], in which the force torques in the ankles were utilized to establish an approximation of the contact in the feet for walking. However, in general, biped applications tend not to measure coefficient of friction at all, preferring to utilize balancing behaviors for slip recovery, and relatively conservative estimates of friction for slip prevention. In most environments, especially those in which robot's are traditionally tested, this is a functional approach. However, as the environments become more complex, the likelihood of stable, predictable and conservative friction estimates dwindles.

This is arguably even more true for hand contacts, since hand-holds, often used as support in the lateral, sagittal, and transverse directions, can be placed in non-gravity normal orientations with vastly greater ease than the feet, due largely to the relatively minimal forces they need produce during locomotion. This orientation makes hands more susceptible to slip, since they can be relied on neither for large normal forces, as the feet can, which would make moderate tangential force, nor for minimally applied tangential forces, as their orientation will primarily dictate the angle of attack of any useful forces at the contact point. In order to both prevent slip and fully utilize the potential of multi-contact control, it is useful to establish a technique for approximating friction parameters before trying to utilize hand contacts for extensive support, ideally in a way that does not require prior knowledge of the environment.

In order to provide a quantifiable visualization of this, consider Figure 5.1. Multi-contact support may potentially increase the available 2D projection of the static support polygon depending on the utilization of forces at the contact points and the pose of the system. Without use of multi-contact forces, the static support polygon is isolated to the external edges of the feet, 5.1b. Adding normal forces in multi-contact support, Figure 5.1c, expands the support polygon from its base, Figure 5.1b, by an additional 42%. However, adding use of both the normal and tangential forces, Figure 5.1d, at the hand contact location expands the region of support by 91% of the region original foot-only support polygon.

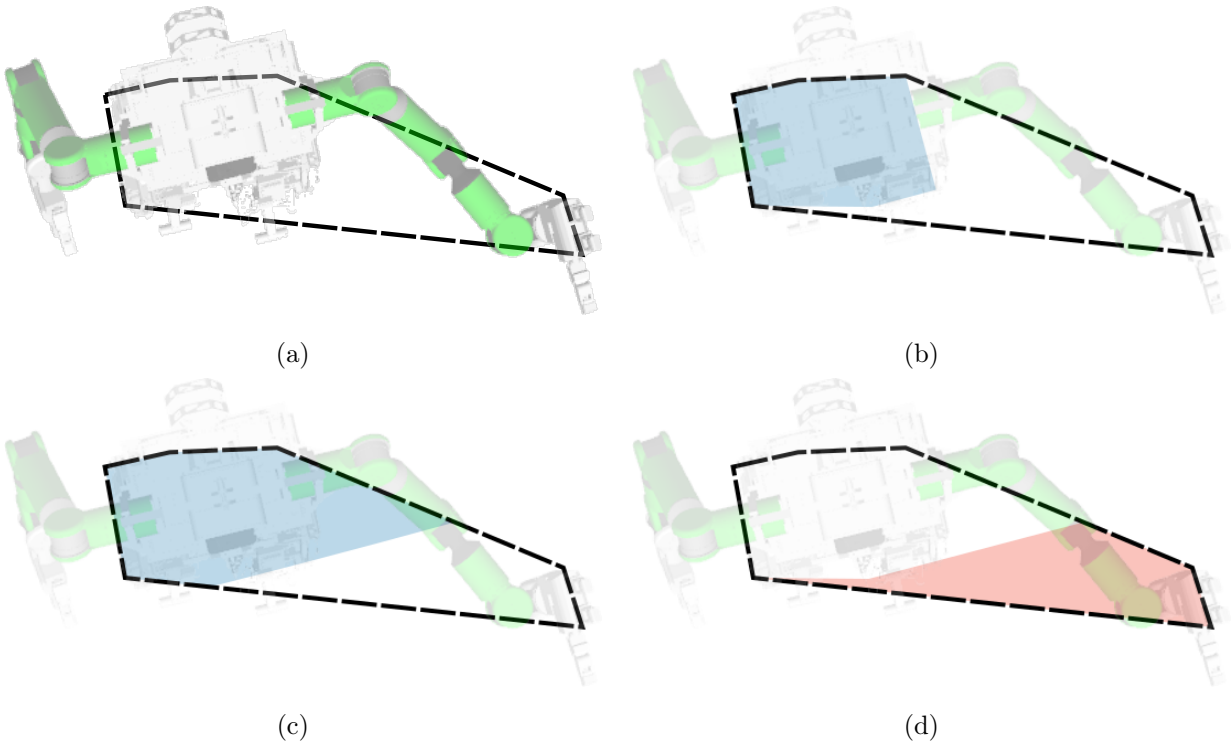


Figure 5.1: With added multi-contact support, the COM can be statically moved outside the base support polygon of the feet (b) to anywhere within the contact points established by the feet and hands (a). However, in the orientation specified, the polygon can be expanded using multi-contact and normal forces (c), but some areas of the support polygon are unreachable statically without use of tangential forces at the hand contact location (d)

These numbers somewhat inflated by the assumption of $\mu_s = \infty$, and the actual area of increase is also largely based on the robot's orientation. Despite this arbitrariness, Figure 5.1 does provide proof that use of multi-contact control and tangential forces could create significant improvement in the overall support statically available to the platform.

5.2 Formulation of the Friction Estimation Technique

5.2.1 Friction Law

Dry friction is the characterization of force that opposes movement from one surface sliding across another surface, dictated by Coulomb's Law of Friction. This states that slip will not occur when the tangential force is less than the available frictional force between two

objects.

$$F_T \leq \mu_s F_N, \quad (5.1)$$

where F_T is tangential static friction force, μ_s is the coefficient of static friction, and F_N is the normal force between the two objects. Based on this representation, the static friction coefficient can be determined through the relationship between normal and tangential forces in the maximally loaded no-slip condition, when F_T is equal to the available frictional force. Though there are exceptions to these rules in the case of wet friction, for the purposes of this technique dry friction is assumed.

5.2.2 Force Detection with the Disturbance Model

Though it would be simplest to directly measure applied forces at the hands with their own dedicated force-torque sensors, many platforms ESCHER included, lack this hardware. This is primarily due to the relatively new application of multi-contact balance to robots, as well as a deplorable lack of recognition for the usefulness of such a device. However, it is worth noting that the addition of said sensors could create difficulties in other areas. Force-torque sensors are large and often expensive, and their addition to any existing platform would likely require a complete remodel of the arm/hand hardware to accommodate what a less than critical piece of equipment.

Lacking this sensor then, hand forces must be measured elsewhere. As observed in [49], it is possible to detect the magnitude and direction of a disturbance force if a number of assumptions are made, primarily that only one force is being applied to the platform. This disturbance force may be measured according to

$$M\ddot{\mathbf{x}}_{\text{cog}} = {}^{\text{cog}}\mathbf{T}_c \mathbf{f}_c + {}^{\text{cog}}\mathbf{T}_{\text{dist}} \mathbf{f}_{\text{dist}} + M\mathbf{g}, \quad (5.2)$$

where M is the system mass, $\ddot{\mathbf{x}}_{\text{cog}}$ delineates the acceleration of the center of gravity, ${}^{\text{cog}}\mathbf{T}_c \mathbf{f}_c$ is the transform from the frame of contact force \mathbf{f}_c to the center of gravity frame, ${}^{\text{cog}}\mathbf{T}_{\text{dist}}$ is the transform from the frame of the disturbance force, \mathbf{f}_{dist} to the center of gravity frame and g is the gravity matrix.

To extrapolate the hand forces for the proposed friction approximation technique, this equa-

tion can be reformulated to calculate any unknown contact force, for example a single additional contact with the hand, \mathbf{f}_{hand} ,

$$\mathbf{f}_{\text{hand}} = {}^{\text{hand}}\mathbf{T}_{\text{cog}}(M(\ddot{\mathbf{x}}_{\text{cog}} - \mathbf{g}) - {}^{\text{cog}}\mathbf{T}_{\text{foot},l}\mathbf{f}_{\text{foot},l} - {}^{\text{cog}}\mathbf{T}_{\text{foot},r}\mathbf{f}_{\text{foot},r}), \quad (5.3)$$

where ${}^{\text{hand}}\mathbf{T}_{\text{cog}}$ is the transform from the CoG frame to the frame of \mathbf{f}_{hand} , $\mathbf{f}_{\text{foot},l}$ and $\mathbf{f}_{\text{foot},r}$ are the measured force values of the left and right foot respectively, transformed to the CoG frame by their respective transforms ${}^{\text{cog}}\mathbf{T}_{\text{foot},l}$ and ${}^{\text{cog}}\mathbf{T}_{\text{foot},r}$.

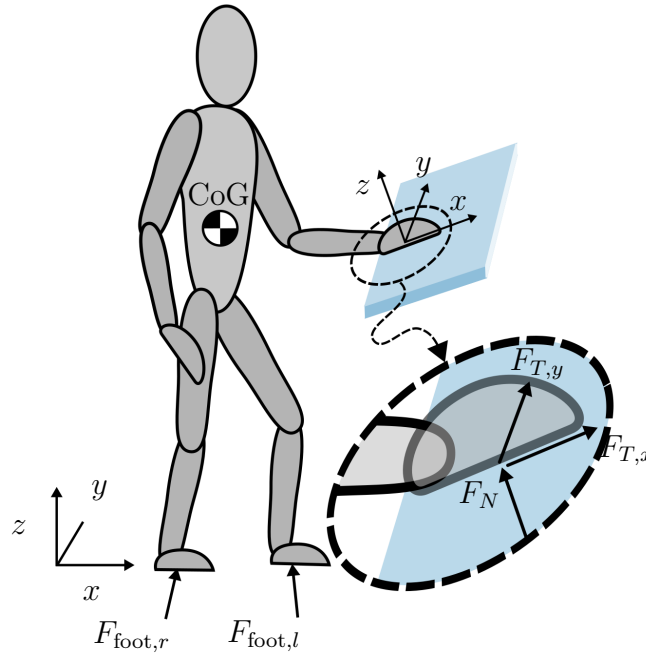


Figure 5.2: Illustration of humanoid robot contact frames [1].

5.2.3 Slip Detection from Applied Force

The relationship between tangential force and normal force, as in [50], can be used to detect a slip in two surfaces. When the amount of desired applied tangential force exceeds the available resistive friction force, slip will occur, causing a noticeable drop in the measured value of F_T . We use slip detection to find the maximum value of F_T over some series of discrete measurements of tangential force with timestep t ,

$$\mu_s = \frac{\max(F_{T,t})}{F_{N,t}}. \quad (5.4)$$

Since slip, and therefore the maximum value of F_T cannot be determined until after slip has occurred, and therefore F_T has decreased, our approach must record and evaluate data such that a maximum value may be determined after having been measured.

It is worth noting that, during this technique, absolute detection of maximum F_T is potentially confounded by stick-slip behavior. In an ideal system, once maximum frictional force has been achieved the resulting movement will continue applying force equal to the kinetic friction force; however, in physical practice, this movement is more likely to involve stick-slip behavior, where alternating loads of static and kinetic frictional forces occur, resulting in a sinusoidal wave in the measured value of F_T between the static friction force and the kinetic friction force. However, since this approach is only dependent on determining a local maximum in F_T , this should not confound the proposed algorithm, though it could potentially lead to longer measurement times.

5.2.4 Formulation of the Friction Approximation Technique

Combining Equations 5.3 and 5.4, the central formulation for this technique emerges,

$$\mu_s = \frac{\max(S_T(M(\ddot{\mathbf{x}}_{\text{cog}} - g) - {}^{\text{cog}}\mathbf{T}_{\text{foot},l}\mathbf{f}_{\text{foot},l} - {}^{\text{cog}}\mathbf{T}_{\text{foot},r}\mathbf{f}_{\text{foot},r}))}{S_N(M(\ddot{\mathbf{x}}_{\text{cog}} - g) - {}^{\text{cog}}\mathbf{T}_{\text{foot},l}\mathbf{f}_{\text{foot},l} - {}^{\text{cog}}\mathbf{T}_{\text{foot},r}\mathbf{f}_{\text{foot},r})}, \quad (5.5)$$

where \mathbf{S}_T and \mathbf{S}_N are selection matrices for the tangential and normal forces, respectively. Equation 5.5 allows the approximation of the applied hand forces from Equation 5.3 to be utilized in Equation 5.4 in accordance with Coulomb's Law of Friction. This equation is reliant on two major assumptions for general application: first, that, at measurement, the only disturbance force is provided by the hand – there is no additional unmeasured force applied to the system – and second, that the friction coefficient at the hand is uniformly distributed, with no variation depending on applied force direction or contact moment.

In order to fully utilize 5.5 to estimate the desired slip point, the following iterative algorithm is employed to determine the maximum friction force prior to slip:

where desired applied normal force, $F_{N,d}$ is specified to the algorithm, and the tangential force $F_{T,d}$ is incremented by step size, k , where $\mathbf{f}_{e,d}$ and $\mathbf{f}_{e,m}$ delineate the desired and measured forces at the end effector(s), respectively.

Algorithm 1 Incremental Friction Approximation

```

1: procedure FRICTIONAPPROX( $F_{N,d}, k$ ) ▷ estimate  $\mu_s$ 
2:    $F_{T,max} = 0$  ▷ set  $F_T$  to some low initial value, i.e  $\mu_s \approx 0$ 
3:   do
4:      $F_{T,d} = F_{T,d} + k$  ▷ increment  $F_{T,d}$  by  $k$ 
5:      $\mathbf{f}_{e,d} = \begin{bmatrix} 0 & F_{T,d} & F_{N,d} & 0 & 0 & 0 \end{bmatrix}$ 
6:     whole_body_controller.set( $\mathbf{f}_{e,d}$ )
7:     update_sensors() ▷ update  $\ddot{\mathbf{x}}$  and  $\mathbf{f}_{base,m}$ 
8:      $\mathbf{f}_{e,m} = {}^e\mathbf{T}_{cog}(M\ddot{\mathbf{x}} - {}^{cog}\mathbf{T}_b\mathbf{f}_{base,m} - Mg)$ 
9:      $F_{T,m} = \mathbf{f}_{e,tangential}$ 
10:     $F_{N,m} = \mathbf{f}_{e,normal}$ 
11:    while  $F_{T,m} < F_{T,max}$  ▷  $F_{T,m} >$  than previous
12:     $\mu_s = F_{T,m} \div F_{N,m}$  ▷ Equation 5.4
13:    return  $\mu_s$ 

```

5.3 Three-Link Simulation

We consider a three-link planar robot constructed using the Robotics Toolbox [67], configured to touch a non-gravity normal plane. In humanoids, hand contacts are typically used as largely secondary balance limbs, with primary support being provided by the legs. As such, the portion of the normal force at the base foot is significantly greater than that applied at the hand. This is reflected in the three link model by limiting maximum total force at the end effector, and by considering the base link, the foot, to have sufficient total normal force to avoid slip itself. In such a case, the base joint may be considered fixed, with net force values measured at this point. For the purpose of this simulation, each link is 0.432 m long, and at an evenly-distributed 17.4 kg.

Following Algorithm 1, with an initial $F_{N,d}$ applied, the tangential force is increased from 0 N until slip is detected in increments of $k = 0.10$ N, 0.20 N, and 0.55 N. Tangential force is increased over the a 1 second period and measured at the end of each period. Slip detection is indicated by the point at which the measured $F_{T,m}$ value at the base link is less than the previous $F_{T,m}$ value, indicating a transition between the static friction and kinetic friction states, since kinetic friction force is less than its static counterpart. Once initial slip has been detected at the maximum $F_{T,m}$ value, utilizing Equation 5.4, the friction coefficient is

determined by the maximum resultant force.

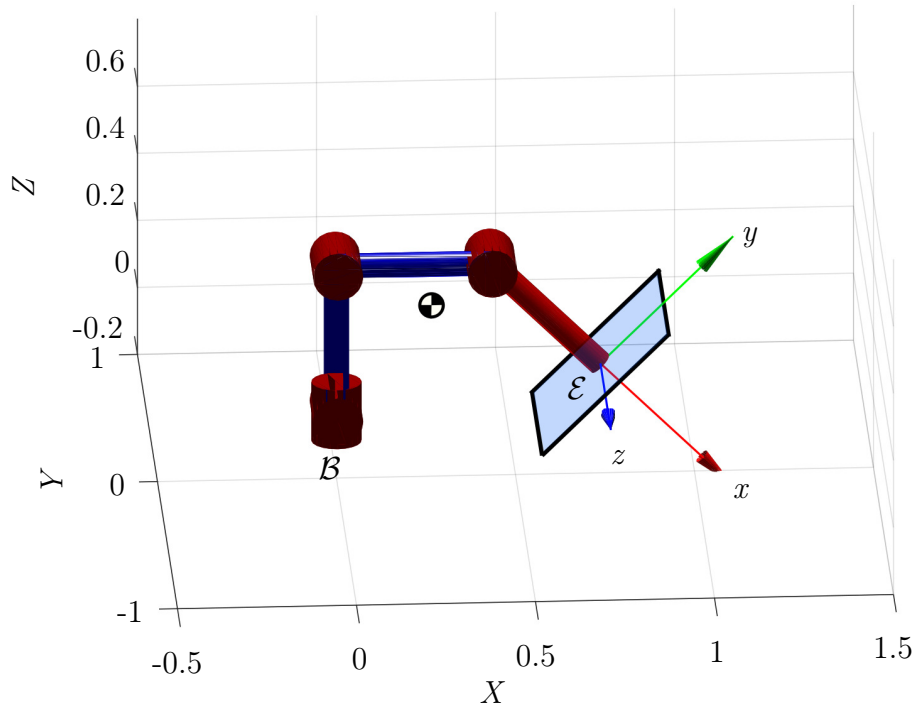


Figure 5.3: A simple 3-link model was developed to simulate a robot with fixed base \mathcal{B} pushing on a non-gravity normal surface at the end effector, \mathcal{E} [1].

5.3.1 Simulation I - Simulation of Different Increment Sizes

In Figure 5.4, the friction coefficients, chosen arbitrarily to represent physical imprecision, are $\mu_s = 0.36125$ and $\mu_k = 0.19125$. The initial experiment, 5.4 shows an $F_{N,d}$ of 5 N, so slip occurs when $F_T = 1.80625$ N. Step size is a factor in this simulation, as the higher k value ends up with a greater error (8.7%) compared to the other two smaller step sizes (0.346%). These results indicate that increasing k , the rate at which F_T is increased, causes the algorithm less accurate than use of a smaller k , though small k values have a longer execution time.

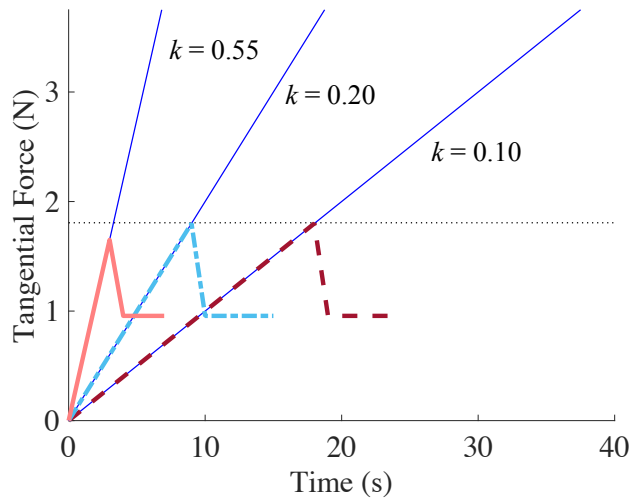


Figure 5.4: The blue lines indicate the desired F_T for each set of force increments, k . Increasing the step size results in less accuracy in the measurement, though execution time is significantly decreased. In general, all three values of k manage to come within 10% of the actual value of μ_s .

5.3.2 Simulation II - Increasing the Desired Normal Force

To counter the inaccuracies of a high k , in the second simulation, Figure 5.5, the normal force is increased to 20 N, therefore increasing the magnitude of the slip value for F_T . The resultant measurements are generally either the same or more accurate, (error of 0.346%, 0.346%, and 1.03% for $k = 0.1, 0.2,$ and 0.55 respectively). While this increased normal force causes the larger step size ($k = 0.55$) to be more accurate, all of the step sizes take more time than in the previous simulation. It is also worth noting that, in this paper's proposed

application, use of large forces at the hand contact can lead to potentially dangerous results when slip does occur, with the resulting imbalance affecting the entire system.

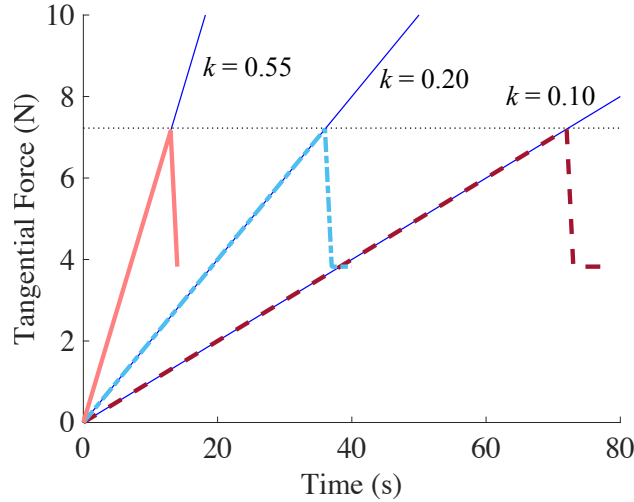


Figure 5.5: The blue lines indicate the desired F_T for each set of force increments, k . Increasing the step size results in less accuracy in the measurement, though execution time is significantly decreased. In general, all three values of k manage to come within $< 2\%$ of the actual value of μ_s .

5.3.3 Simulation III - Approximation with Similar Coefficients

For the third simulation, Figure 5.5, the normal force is returned to 5 N, but the friction values are changed to $\mu_s = 0.30020$ and $\mu_k = 0.25001$. The proximity of μ_s and μ_k limits the maximum error of the system, as the settling kinetic friction force value is only 16.7% below the correct static friction force. As in Figure 5.4, the results indicate that increasing step size leads to less accurate approximate friction values (error of 0.067%, 6.73%, and 16.7% for $k = 0.1$, 0.2, and 0.55 respectively). While step size is not the primary factor in this process, these results indicate that raising F_T too quickly causes inaccuracies in the measured values. It is worth noting that, due to the relationship between static and kinetic frictional forces, Algorithm 1 should never overestimate the frictional value of the surface, though the magnitude of its underestimation may be largely dependent on the difference between μ_s and μ_k . Quantitative results from Figures 5.4, 5.5, and 5.6 are shown in Table 5.1.

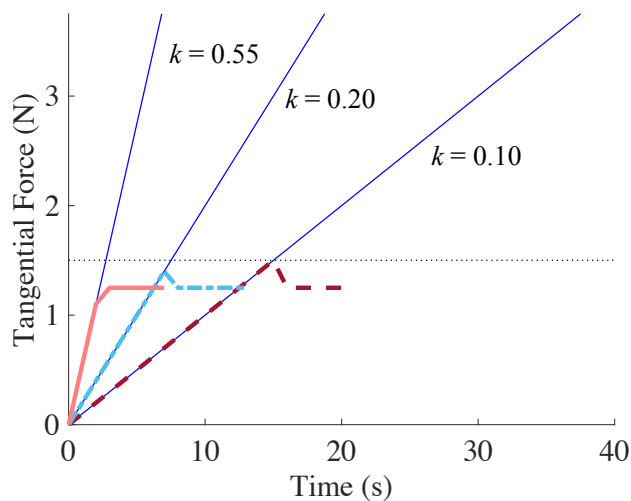


Figure 5.6: The blue lines indicate the desired F_T for each set of force increments, k . Operating with 5 N of normal force, and the lowest μ_s of all the simulations, this test resulted in the most inaccuracy across all step sizes. Inaccuracy is somewhat mitigated by the proximity of μ_s and μ_k , and the tendency of this algorithm is to underestimate rather than overestimate, so inaccuracies still will not cause slip.

Table 5.1: Results of 3 Link Simulation(Figures 5.4, 5.5, and 5.6)

Simulation	$F_{N,d}$ (N)	k (N)	Actual μ_s	Actual μ_k	Measured μ_s
I	5	0.01	0.36125	0.19125	0.360
	5	0.02	0.36125	0.19125	0.360
	5	0.55	0.36125	0.19125	0.330
II	20	0.01	0.36125	0.19125	0.360
	20	0.02	0.36125	0.19125	0.360
	20	0.55	0.36125	0.19125	0.358
III	5	0.01	0.30020	0.25001	0.300
	5	0.02	0.30020	0.25001	0.280
	5	0.55	0.30020	0.25001	0.250

5.4 Implementation on the ESCHER Platform

The approach from Section 5.2 was then expanded beyond the three-link model in Section 5.3 to the ESCHER Model. ESCHER is Virginia Tech’s 38 DoF torque-controlled, compliant humanoid robot. With the multi-contact approach developed in Chapter 4, the robot is able to use its hands to balance and support its body weight on surrounding surfaces. This functionality may be further extended by adopting Algorithm 1 with slight modifications, to estimate friction parameters at the hand contact point. With F_e as F_{hand} and the base force measurement F_{base} as a combination of both $F_{\text{foot},l}$ and $F_{\text{foot},r}$, and utilizing appropriate transform matrices for each of these points, the algorithm proposed above may be applied to the humanoid model. The additional degrees of freedom between the simple model and the humanoid model lead to more system noise, due to reliance on more encoders and sensors, but the base formulation remains unchanged.

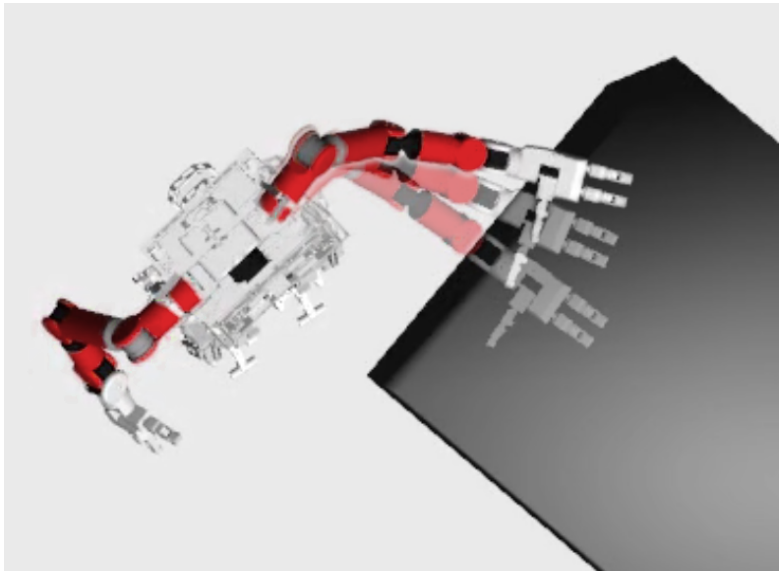


Figure 5.7: ESCHER’s hand is moved laterally away from the body to apply tangential force to the contact surface.

5.4.1 Layout of the Simulation Environment

The simulated model of ESCHER was placed in a Gazebo Simulation[68] and navigated to a position 1.0 m behind a box of height 1.2 m. The actual friction coefficient between the box

and the robot’s hand was set to $\mu_s = 0.50$ in the simulation environment. The measurement submodule was applied to the system, resulting in the execution of the programmatic implementation of Algorithm 1. With an initially applied desired normal force of 15 N, a purely normal contact was initiated within the multi-contact whole body controller. After load was initiated, the robot was directed to increase the applied tangential force at the hand contact in the y direction, as defined in Figure 5.2. With a step size k of 0.5 N, the tangential force was increased while monitoring the system for slip.

The CoG acceleration, $\ddot{\mathbf{x}}_{\text{cog}}$, as noted in [49], can be a complicated measurement to explicitly take, as the CoM shifts between linkages as the system moves, so no individual instrument can be utilized to measure it. For the purposes of ESCHER’s momentum controller, $\ddot{\mathbf{x}}_{\text{cog}}$ was approximated from an equal fusion of the Kalman-filtered acceleration vector from the onboard inertial measurement unit (IMU), located at the pelvis, and the calculated CoG acceleration derived from the joint states and rigid body dynamics of the system. To clean up the received force torque data, signal from the ankle sensors was processed through a low-pass filter to limit signal noise.

5.4.2 ESCHER Simulation Results

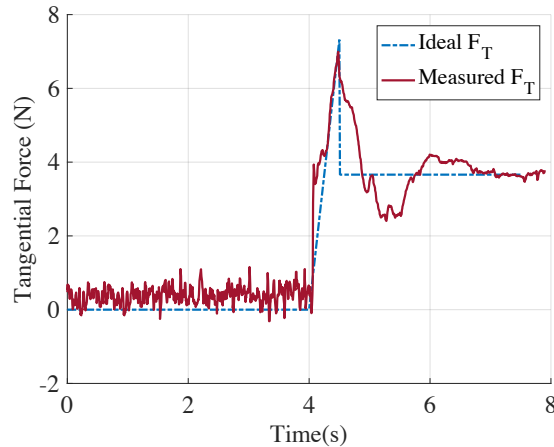


Figure 5.8: In the ESCHER Simulation, the maximum F_T achieved was 7.04 N (top). Though the setpoint force for F_N force was 15 N, at the maximum value of F_T , just before 4.5 s, the normal force was measured at, 14.64 N for a calculated $\mu = 0.481$, compared to the actual value, 0.500

The proposed estimation technique was applied, with results shown in Figure 5.8. With the increased imprecision of the 38 DoF system, there was noticeable noise, as well as the

beginnings of stick-slip behavior in the resulting measured F_T . Once the applied normal force, with desired value 15 N, stabilized, the tangential force was incremented. With a step size k of 0.5 N, the maximum measured F_T occurred just after 4 seconds at 7.04 N. At this time, the normal force was measured at 14.64 N, 2.4% less than the target value of 15 N, due to the system noise and associated error in the whole body controller. Based on this point the estimated value of $\mu_s = 0.481$ was 3.8% lower than the actual value of 0.5.

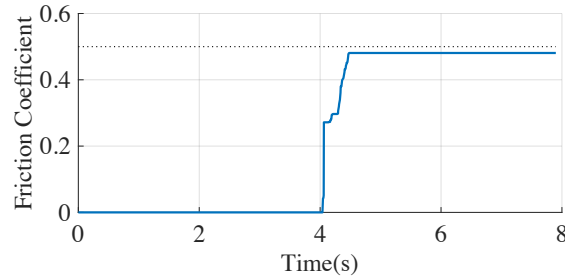


Figure 5.9: Maximum friction coefficient is continuously calculated based on the measured F_T and Equation 5.3.

Concurrently with the measurements from Figure 5.8, the coefficient of static friction is calculated online as in Figure 5.8. Its maximum value is dependent on the peak F_T , which limits noise in the μ_s measurement, as it can never decrease during approximation. This means that, were it implemented on a real-time system, it could provide consistency, but also makes it slightly susceptible to overestimates due to system noise, if it is approximately close to the proper μ_s otherwise.

Simulation with a higher k of 2 N, (Figure 5.10) results in less precision, and, though no discernible relationship between k and stick-slip behavior has been observed, this figure provides a look at the effects of said behavior on the max value of F_T . In this example, the measured value of F_T was 6.35 N, making a friction coefficient of 0.429, an error of 14.2%.

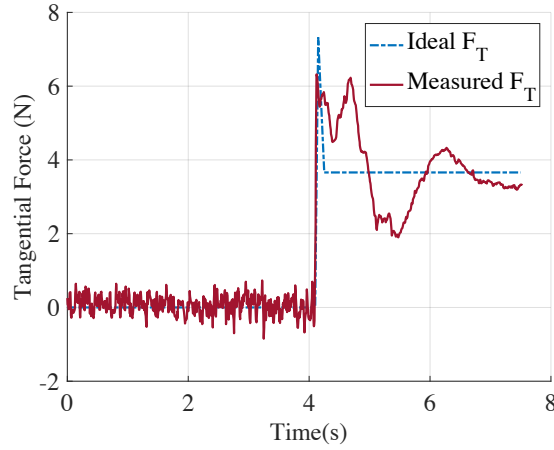


Figure 5.10: Not all measurements were consistently clean, with potential stick slip behaviors challenging the maximum F_T measured. The maximum F_T here is 6.35 N for a μ_s of 0.429 at a k of 2 N.

5.4.3 Significance of Humanoid Friction Measurements

Due to the increased noise due to sensor data, the increased DoF, and the potential for stick-slip behaviors discussed in Section 5.2.3, additional modification to Algorithm 1 was required. First, to ensure that noise did not cause an invalid local maximum, the max value was required to stay as the highest F_T for a 3.5 second duration. The result of this was that, after slip had occurred, continued stick slip behavior realized as waves in the otherwise constant kinetic friction force were observed. More practically, this meant that measurement time was significantly increased, which limits the in-field utility of this technique. Additionally, this continued sliding, for which the whole body controller does not account, is potentially dangerous behavior. Any dynamic movements not expected by the whole body controller are deemed disturbances, for which there are compensatory behaviors, but may still cause potential falls. For this reason, normal force, and by proxy maximum allowable tangential force, are kept to a minimum. While this does limit the potential accuracy of the measurement technique, it provides a safer basis for the system's operation.

As mentioned earlier, since the kinetic friction coefficient is consistently less than the static friction coefficient, and the minimum possible estimated value in a successful measurement of any step size occurs at $F_T = F_{\text{friction}}$, where F_{friction} is the kinetic friction force, the minimum estimation for any μ_s based on Algorithm 1 should be $\mu_{s,m} = \mu_k$. This value, though still limiting to the potential area of support for the system, is still a viable support point that

will avoid slip, which is the goal of this technique. If, for any of a number of reasons, slip is overestimated, either by error in the measurement functionality or by a violation of one of the primary assumptions of this technique, (friction uniformity, no additional force disturbances, etc.) friction coefficient may be re-estimated, or simply reduced until slip no longer occurs.

5.4.4 Offline ESCHER Hardware Implementation

Due to the degree of positional imprecision present on the actual robot arms, limitations were present on the ability of the robot to exhibit the same degree of multi-contact control as was achieved in simulation. For that reason multi-contact experimentation on the actual platform was limited to an offline implementation, which validates the underlying methodology, if not the direct implementation. It was possible to run an unconstrained friction estimation on the actual platform in accordance with the previous section. The results of that experiment are discussed in the following subsections.

5.4.5 ESCHER Hardware Setup

As in Section 5.4, the robot was placed behind a box of height 1.2 m. It was directed to make contact with the palm of the right hand against the box and apply normal force to the box's surface. Once sufficient normal force was achieved, tangential force was manually incremented until slip occurred. Unlike the previous implementation, this measurement process was teleoperated, leading to an uncertain rate of k increase. Despite this, since none of the underlying assumptions of Equation 5.3 were violated, the data still provide an approximation of the friction coefficient between the robot's palm pad and the wooden surface of the box.

5.4.6 Establishing Baseline Friction

In order to establish a comparative friction coefficient for this measurement process, the actual friction coefficient of the contact was estimated prior to the robot measurement. This measurement is relatively simple to do if precision is not vital. As has commonly been observed, static friction coefficient can be measured between two surfaces using an inclined

plane using,

$$mg \sin \theta = \mu_s mg \cos \theta \quad (5.6)$$

where m is the sliding object mass, g is gravity, and θ refers to the angle of inclination. If θ is increased until the point at which slip occurs, this equation can be simplified to

$$\mu_s = \tan \theta \quad (5.7)$$

So then, by placing ESCHER's palm plate, which is removable, on a sheet of the same wood used for testing, sliding behavior can be initiated by increasing the angle of the support surface, the wood. Three separate trials of this resulted in a measured angle of $\theta = 40.8^\circ$,

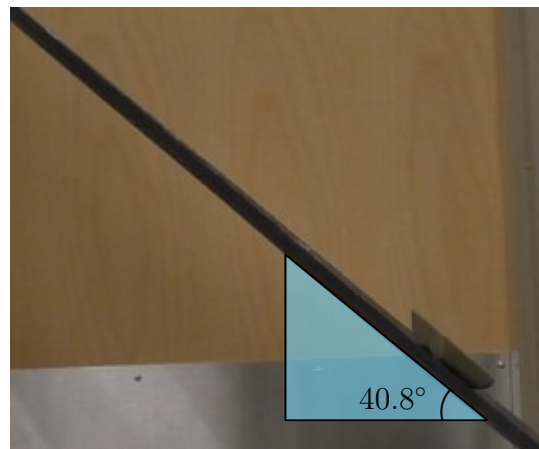


Figure 5.11: The palm plate (bottom right) slides down a sheet of wood at 0.712 rad (40.8°) for a measured friction coefficient of $\mu_s = 0.863$

corresponding to a friction coefficient of $\mu_s = 0.863$. This is in keeping with the expected range of values for rubber against various surfaces (0.56-1.15) [69]

5.4.7 Friction Measurement with the ESCHER Platform

Reorientation of the hand during measurement due to manual operation resulted in inconsistent use application of F_N . Additionally, there is significant observable noise in the actual sensors, resulting in a degree of imprecision that proves significant to the overall measurement. After offline execution of Algorithm 1, the resultant maximum F_T was 5.48 N, with a

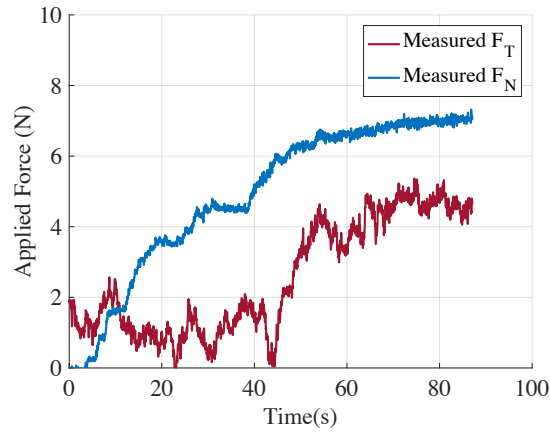


Figure 5.12

corresponding F_N of 7.18 N, resulting in a μ_s of 0.763, a 12% error based on the value calculated in Section 5.4.6. Based on the algorithm proposed, the error is largely arbitrary, as the traditional peak is not appropriately represented, and normal force is not held constant.

The noise and error of this measurement are significant, and overall slip behavior is inconsistent with the earlier simulations, as stick slip behavior kept the overall shape of the F_T curve from taking the characteristic dip observed for kinetic friction in the previous plots. This is likely due both to manual operation and to the natural compliance of the robot, which is not accurately represented in the simulation or the rigid body dynamics. Based on these, these results do not strictly confirm the accuracy of the measurement by any means, with the noticeable system error and noise obscuring the actual practical performance of the algorithm.

However, this method does again successfully establish a friction coefficient value that, while inaccurate compared to the prior simulation values, is an underestimate of the actual value of μ_s and therefore will not cause slip. Additionally, this experiment verifies the validity of Equation 5.3 as an approximation of applied forces at the sensor-less right hand.

5.5 Quantification of Friction Results

It is useful here to provide a quantitative example of how such knowledge would not only reduce the likelihood of slip, as is maintained by the whole body controller's use of the

constraint pyramid of the generalized contact forces, ρ , but also potentially expand the region of support. This was demonstrated briefly in Figure 5.1, but for the case of an infinitely large μ_s . For the purpose of quantifying the improvement of the measurements from this section, we will briefly consider the example shown in Figure 5.13.

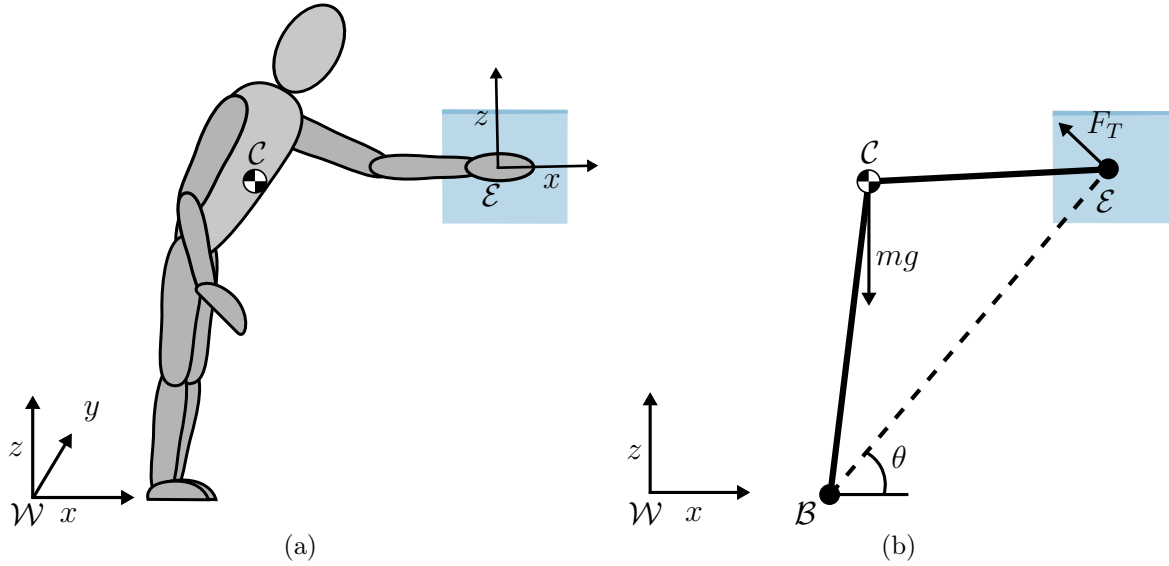


Figure 5.13: In a tangential force reliant posture (a), the rigid body representation of the robot's applied forces may extend its center of mass, \mathcal{C} , past the ends of its feet, \mathcal{B} , along the x -axis if the moment induced about this point of rotation by the end effector \mathcal{E} from force F_T is greater than or equal to the moment created by the rotation of \mathcal{C} about \mathcal{B} .

In Figure 5.13a, a humanoid is placed in a multi-contact orientation with its left hand applying force to a wall perpendicular to the sagittal plane of the body. This hand is located at some point $\mathbf{r}_{\mathcal{E}}$ in the world frame \mathcal{W} . It is able to apply force at that location in the tangential directions defined by x and z . Simultaneously, the CoG, \mathcal{C} is moved forward along the world frame x axis to point $\mathbf{r}_{\mathcal{C}}$. In order to maintain the CoG inside the 2D projection of the static stability region and not pivot into a fall about the point of rotation at the tip of the feet, \mathcal{B} , the resistive moment induced by the hand force, F_T , must be equal to the moment created about the base by the CoG. So, in this case,

$$\mathbf{r}_{\mathcal{E}} F_T = m g \mathbf{r}_{\mathcal{C}}. \quad (5.8)$$

To balance this expression for moments about the y axis, there is some maximum distance in the x direction that $\mathbf{r}_{\mathcal{C}}$ may travel, and a corresponding minimum required F_T to achieve that

distance. The minimum required tangential force is that which is orthogonal to the vector between $\mathbf{r}_{\mathcal{E}}$ and $\mathbf{r}_{\mathcal{C}}$ in the xz -plane, as in Figure 5.13b. The relationship between friction coefficient and the forward statically stable rection is expressed then as,

$$x_{\mathcal{C}} = \mu_s \frac{F_N(x_{\mathcal{E}} \cos \theta + z_{\mathcal{E}} \sin \theta)}{mg}, \quad (5.9)$$

where θ is the angle between horizontal plane and the line connecting the rotation point \mathcal{B} and the end effector \mathcal{E} . Though this is applicable to any multi-contact pose that the robot might utilize in this orientation, for the sake of quantification, we will consider a pose where both feet are side by side and the left hand is in contact at $\mathbf{r}_{\mathcal{E}} = (0.4, 0.4, 1.2)$, and $\mathbf{r}_{\mathcal{B}} = (0.0, 0.0, 0.0)$. This pose may be seen as the hand and foot locations in Figures 5.14a and 5.14a below.

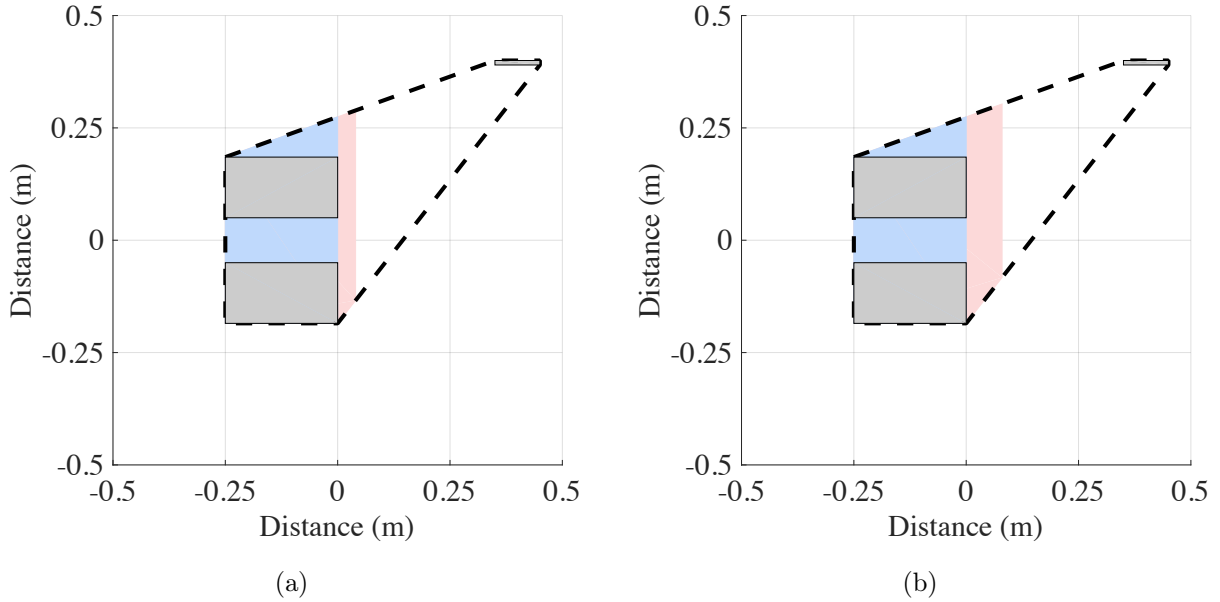


Figure 5.14

The standard preprogrammed value for μ_s of 0.2 is shown in 5.14a. The blue region indicates the region in which the robot can statically operate without utilizing any tangential forces at the hand. When tangential forces are applied but the maximum net applicable force allowed at the hand is 150 N, the red region is also statically available. In the case of

$\mu_s = 0.2$, the static support polygon is expanded by 17% of the normal-force-only polygon. By increasing from $\mu_s = 0.2$ (Figure 5.14a) to $\mu_s = 0.5$ (Figure 5.14b), the static stability region is increased by about 33%.

So then, comparing the total area of the region of support that is potentially available compared to the region of support available with the measured μ_s from ESCHER's simulation of $\mu_s = 0.481$, which would result in an increase of about 32% the reduction in support region is less than 1%. So, though the accuracy of the system is not perfect, resulting in some level of error, it is still able to increase the humanoid's support region by a third without significant risk of overestimation and slip.

Chapter 6

Conclusion and Future Work

The purpose of this paper was to present the adaptation of a bipedal model optimization to include multi-contact functionality. This was established based on the accepted formulations for the compliant robot’s whole body controller, and tested on the humanoid platform *ESCHER*. The usability of this multi-contact model was then extended to establish a novel technique for estimating friction coefficients in bipedal platforms with ankle-mounted force torque sensors. This functionality was achieved using both a simple three link model in MATLAB simulation, and using the time-varying DCM model optimization controller established for the *ESCHER*’s previous operation. The robot applies force with its hand via the whole body controller to a surface and, by iteratively incrementing the applied tangential force at the hand, detects slip based on maximum tangential force achieved. Forces utilized for this approximation are indirectly measured by the foot sensors, and the estimated value of the static friction coefficient is measured. This value is utilized by the robot’s whole body controller to establish an accurate model of the support region, allowing the robot to avoid slip at the hand contacts by reducing use of tangential forces at that point, or expand the usable support region by increasing the allowable tangential forces at that point. Balancing and control is still provided by the model optimization already established in *ESCHER*’s control software.

As shown in Chapter 5, this method is able to produce usable estimates of the static friction coefficient, but results are largely based on simulation, as hardware performance lagged behind the performance of the Gazebo simulation. This is largely due to the backlash inherent to the HDT arms used for this experiment. It is anticipated that the new model of

arms, set to be attached to the robot soon, will address these concerns and provide improved performance for coefficient measuring using this technique. However, before this technique can be relied upon in the field, it is necessary to reduce the measuring time of the friction coefficient; humans are able to perform estimation of the surface parameters as contact is initiated, and decreasing the performance time of this process would provide a great deal of in-field utility.

This performance time could be reduced by the fusion of the acquired friction coefficient data with the other sensory information and object recognition available on the robot platform. The measured friction coefficient could be applied to objects or surfaces in concurrence with Simultaneous Localization and Mapping to prevent the robot from re-measuring a surface. Additionally, object recognition combined with machine learning could allow the robot to recognize types of surfaces, categorizing what it sees friction coefficients it has measured before. In this way, the required testing time could be dramatically diminished, either by assuming that categorized surfaces will perform similarly, or by using an assumed value as a starting point, and this removing the need to increment all the way from zero tangential force to the maximum tangential force.

Though accurate friction coefficient estimation is not perceived as critical to locomotion, it does vastly expand the performance capabilities of the platform. Not only does it prevent slip and provide a more accurate understanding of the available region of support, it also allows the initiation of deliberate sliding behaviors. As in [53], deliberate contact sliding is regularly used by humans during locomotion. This can be easily extended beyond the feet to the hands, where humans use light sliding as normal support on stair railings to create an additional support point that is not statically fixed to the surrounding environment. Accurate knowledge of the friction coefficient could provide the basis for establishing research in the area of sliding hand supports.

Bibliography

- [1] Cameron P. Ridgewell, Robert J. Griffin, Tomonari Furukawa, and Brian Lattimer. Online estimation of friction constraints for multi-contact whole body control. In *IEEE-RAS International Conference on Humanoid Robots, 2017 (submitted)*.
- [2] Karthik Kappaganthu and C. Nataraj. Optimal Biped Design Using a Moving Torso: Theory and Experiments. *Biped Robots*, 2011.
- [3] Neo Ee Sian, Takeshi Sakaguchi, Kazuhito Yokoi, Yoshihiro Kawai, and Kenichi Maruyama. Operating humanoid robots in human environments. . . . *for Human Environments*, 2006.
- [4] Darwin G. Caldwell, Nikos Tsagarakis, and Claudio Semini. *Mechanism and Structures: Humanoids and Quadrupeds*, pages 133–153. Springer International Publishing, Cham, 2014.
- [5] Hun-ok Lim and Atsuo Takanishi. Biped walking robots created at Waseda University: WL and WABIAN family. *Philosophical transactions. Series A, Mathematical, physical, and engineering sciences*, 365(1850):49–64, 2007.
- [6] Ichiro Kato. Development of WABOT 1. *Biomechanism*, pages 173–214, 1973.
- [7] I Katoh, M Fujie, T Yoshida, K Ichiryu, and Y Nakano. Development of legged walking robots. *The Hitachi Hyouron*, 68(10):25–30, 1986.
- [8] A. Sano and J. Furusho. Control of torque distribution for the BLR-G2 biped robot. In *Fifth International Conference on Advanced Robotics*, pages 729–734 vol.1, 1991.
- [9] Kazuo Hirai, Masato Hirose, Yuji Haikawa, and Toru Takenaka. The development of Honda humanoid robot, 1998.

- [10] Atlas - the agile anthropomorphic robot.
- [11] Gabe Nelson, Aaron Saunders, Neil Neville, Ben Swilling, Joe Bondaryk, Devin Billings, Chris Lee, Robert Playter, and Marc Raibert. Petman: A humanoid robot for testing chemical protective clothing. *Journal of the Robotics Society of Japan*, 30(4):372–377, 2012.
- [12] Thormang.
- [13] Johannes Engelsberger, Alexander Werner, Christian Ott, Bernd Henze, Maximo A. Roa, Gianluca Garofalo, Robert Burger, Alexander Beyer, Oliver Eiberger, Korbinian Schmid, and Alin Albu-Schäffer. Overview of the torque-controlled humanoid robot TORO. In *IEEE-RAS International Conference on Humanoid Robots*, volume 2015-Febru, pages 916–923, 2015.
- [14] F. Negrello, M. Garabini, M. G. Catalano, J. Malzahn, D. G. Caldwell, A. Bicchi, and N. G. Tsagarakis. A modular compliant actuator for emerging high performance and fall-resilient humanoids. *IEEE-RAS International Conference on Humanoid Robots*, 2015-December:414–420, 2015.
- [15] I.-W. Park and J.-H. Oh.
- [16] Aiman Musa M Omer, Hideki Kondo, Hun-ok Lim, and Atsuo Takanishi. Humanoid Robot HRP-3. *Science And Technology*, pages 48–53, 2008.
- [17] MIOMIR VUKOBRATOVIĆ and BRANISLAV BOROVIĆ. Zero-Moment Point – Thirty Five Years of Its Life. *International Journal of Humanoid Robotics*, 01(01):157–173, 2004.
- [18] Shuuji Kajita, Fumio Kanehiro, Kenji Kaneko, and Kiyoshi Fujiwara. Biped Walking Pattern Generation by using Preview Control of Zero-Moment Point. pages 1620–1626, 2003.
- [19] K Harada, S Kajita, K Kaneko, and H. Hirukawa. ZMP analysis for arm/leg coordination. In *Intelligent Robots and Systems (IRIEEE/RSJ International Conference on*, number October, pages 75–81, 2003.

- [20] Jerry Pratt, John Carff, Sergey Drakunov, and Ambarish Goswami. Capture point: A step toward humanoid push recovery. In *IEEE-RAS International Conference on Humanoid Robots*, pages 200–207, 2006.
- [21] T Takenaka, T Matsumoto, and T Yoshiike. Real time motion generation and control for biped robot -1st report: Walking gait pattern generation. *Intelligent Robots and Systems (IRIEEE/RSJ International Conference on)*, pages 1084–1091, 2009.
- [22] Johannes Engelsberger, Christian Ott, and Alin Albu-Schaffer. Three-Dimensional Bipedal Walking Control Based on Divergent Component of Motion. *IEEE Transactions on Robotics*, 31(2):355–368, 2015.
- [23] Michael A. Hopkins, Dennis W. Hong, and Alexander Leonessa. Humanoid locomotion on uneven terrain using the time-varying divergent component of motion. In *IEEE-RAS International Conference on Humanoid Robots*, volume 2014-Febru, pages 266–272, 2014.
- [24] Michael A. Hopkins, Dennis W. Hong, and Alexander Leonessa. Humanoid locomotion on uneven terrain using the time-varying divergent component of motion. In *IEEE-RAS International Conference on Humanoid Robots*, volume 2015-Febru, pages 266–272, 2015.
- [25] M. H. Raibert and J J Craig. Hybrid Position / Force Control of. *Journal of Dynamic Systems, Measurement, and Control*, 102(June 1981):126–133, 1981.
- [26] Cecil O. Alford and Stanley M. Belyeu. Coordinated Control of Two Robot Arms. *Robotics and Automation (ICIEEE International Conference on)*, pages 468–473, 1984.
- [27] D. Williams and O. Khatib. The virtual linkage: a model for internal forces in multi-grasp manipulation. In *Robotics and Automation (ICIEEE International Conference on)*, volume 1, pages 1025–1030, 1993.
- [28] Luis Sentis, Jaeheung Park, and Oussama Khatib. Compliant control of multicontact and center-of-mass behaviors in humanoid robots. *IEEE Transactions on Robotics*, 26(3):483–501, 2010.
- [29] Jaeheung Park and Oussama Khatib. Contact consistent control framework for humanoid robots. In *Robotics and Automation (ICRA), IEEE International Conference on*, number 1, pages 1963–1969, 2006.

- [30] Oussama Khatib and Luis Sentis. A unified framework for whole-body humanoid robot control with multiple constraints and contacts. *European Robotics Symposium 2008*, pages 303–312, 2008.
- [31] Sang Ho Hyon, Joshua G. Hale, and Gordon Cheng. Full-body compliant human-humanoid interaction: Balancing in the presence of unknown external forces. *IEEE Transactions on Robotics*, 23(5):884–898, 2007.
- [32] Edoardo Farnioli, Marco Gabiccini, and Antonio Bicchi. Optimal Contact Force Distribution for Compliant Humanoid Robots in Whole-Body Loco-Manipulation Tasks. *Robotics and Automation (ICIEEE International Conference on)*, pages 5675–5681, 2015.
- [33] Christian Ott, Maximo a. Roa, and Gerd Hirzinger. Posture and balance control for biped robots based on contact force optimization. In *IEEE-RAS International Conference on Humanoid Robots*, pages 26–33, 2011.
- [34] Bernd Henze, Christian Ott, and Maximo a. Roa. Posture and balance control for humanoid robots in multi-contact scenarios based on Model Predictive Control. In *Intelligent Robots and Systems (IROS), IEEE/RSJ International Conference on*, pages 3253–3258, 2014.
- [35] Edoardo Farniolil, Marco Gabiccini, and Antonio Bicchi. Toward Whole-Body Loco-Manipulation : Experimental Results on Multi-Contact Interaction with the Walk-Man Robot. In *Intelligent Robots and Systems (IRIEEE/RSJ International Conference on)*, pages 1372–1379, 2016.
- [36] Timothy Bretl and Sanjay Lall. Testing static equilibrium for legged robots. *IEEE Transactions on Robotics*, 24(4):794–807, 2008.
- [37] Cyrille Collette, Alain Micaelli, Claude Andriot, and Pierre Lemerle. Dynamic balance control of humanoids for multiple grasps and non coplanar frictional contacts. *the 2007IEEE-RAS International Conference on Humanoid Robots, HUMANOIDS 2007*, pages 81–88, 2008.
- [38] Bernd Henze, Alexander Dietrich, and Christian Ott. An Approach to Combine Balancing with Hierarchical Whole-Body Control for Legged Humanoid Robots. *IEEE Robotics and Automation Letters*, 1(2):700–707, 2016.

- [39] Alexander Werner, Bernd Henze, Diego A. Rodriguez, Jonathan Gabaret, Oliver Porges, and Maximo A. Roa. Multi-contact planning and control for a torque-controlled humanoid robot. *2016 Intelligent Robots and Systems (IRIEEE/RSJ International Conference on (IROS)*, pages 5708–5715, 2016.
- [40] S. Lengagne, Joris Vaillant, Eiichi Yoshida, and Abderrahmane Kheddar. Generation of whole-body optimal dynamic multi-contact motions. *The International Journal of Robotics Research*, 32(9-10):1104–1119, 2013.
- [41] Hitoshi Tamura and Yasushi Kambayashi. Estimation of coefficient of static friction of surface by analyzing photo images. In *Intelligent Decision Technologies*, volume 57, pages 15–26. 2016.
- [42] Norinao Watanabe and Goro Obinata. Grip Force Control Based on the Degree of Slippage Using Optical Tactile Sensor. *Micro-NanoMechatronics and Human Science, International Symposium on*, pages 466–471, 2007.
- [43] Robert D. Howe and Mark R. Cutkosky. Sensing skin acceleration for slip and texture perception. In *Robotics and Automation (ICRA), IEEE International Conference on*, pages 145–150, 1989.
- [44] C. Melchiorri. Slip detection and control using tactile and force sensors. *IEEE/ASME Transactions on Mechatronics*, 5(3):235–243, Sep 2000.
- [45] Chi Zhu and Atsuo Kawamura. What is the real frictional constraint in biped walking? - Discussion on frictional slip with rotation. *Intelligent Robots and Systems (IRIEEE/RSJ International Conference on*, pages 5762–5768, 2006.
- [46] Kenji Kaneko, Fumio Kanehiro, Shuuji Kajita, Mitsuharu Morisawa, Kiyoshi Fujiwara, Kensuke Harada, and Hirohisa Hirukawa. Slip observer for walking on a low friction floor. *Intelligent Robots and Systems (IROS), IEEE/RSJ International Conference on*, pages 1457–1463, 2005.
- [47] J. A. Vázquez and M. Velasco-Villa. Experimental estimation of slipping in the supporting point of a biped robot. *Journal of Applied Research and Technology*, 11(3):348–359, 2013.
- [48] Kwon Ohung and Jong Hyeon Park. Reflex control of bipedal locomotion on a slippery surface. *Advanced Robotics*, 16(8):721–734, 2002.

- [49] Kenji Kaneko, Fumio Kanehiro, Mitsuharu Morisawa, Eiichi Yoshida, and Jean-Paul Laumond. Disturbance observer that estimates external force acting on humanoid robots. *Advanced Motion Control (AMC), 2012 IEEE International Workshop on*, pages 1–6, 2012.
- [50] R. Bayrleithner and K. Komoriya. Static friction coefficient determination by force sensing and its application. *Intelligent Robots and Systems (IRIEEE/RSJ International Conference on*, 3:1639–1646.
- [51] S. Kajita, K. Kaneko, K. Harada, F. Kanehiro, K. Fujiwara, and H. Hirukawa. Biped walking on a low friction floor. In *Intelligent Robots and Systems (IROS), IEEE/RSJ International Conference on*, pages 3546–3552, 2004.
- [52] K. Miura, S. Nakaoka, M. Morisawa, K. Harada, and S. Kajita. A friction based "twirl" for biped robots. *Humanoids 2008 -IEEE-RAS International Conference on Humanoid Robots*, pages 279–284, 2008.
- [53] Kanako Miura, Shin'ichiro Nakaoka, Mitsuharu Morisawa, Fumio Kanehiro, Kensuke Harada, and Shuuji Kajita. Analysis on a friction based "twirl" for biped robots. In *Robotics and Automation (ICRA), IEEE International Conference on*, pages 4249–4255, 2010.
- [54] Zhangguo Yu, Jing Li, Qiang Huang, Xuechao Chen, Gan Ma, Libo Meng, Si Zhang, Yan Liu, Wen Zhang, Weimin Zhang, Xiaopeng Chen, and Junyao Gao. Slip prevention of a humanoid robot by coordinating acceleration vector. *Information and Automation (ICIA), IEEE International Conference on*, (July):683–688, 2014.
- [55] Robert J Griffin, Alan Asbeck, and Alexander Leonessa. Disturbance Compensation and Step Optimization for Push Recovery. *Intelligent Robots and Systems (IRIEEE/RSJ International Conference on*, page Submitted, 2016.
- [56] Gary N. Boone and Jessica K. Hodgins. Slipping and tripping reflexes for bipedal robots. *Autonomous Robots*, 4(3):259–271, 1997.
- [57] Michele Focchi, Victor Barasuol, Marco Frigerio, Darwin G. Caldwell, and Claudio Semini. Slip Detection and Recovery for Quadruped Robots. *International symposium on robotics research*, (September):1–16, 2015.

- [58] Michael A. Hopkins, Dennis W. Hong, and Alexander Leonessa. Compliant locomotion using whole-body control and Divergent Component of Motion tracking. In *Robotics and Automation (ICRA), IEEE International Conference on*, pages 5726–5733, 2015.
- [59] G.A. Pratt and M.M. Williamson. Series elastic actuators. 1:399–406.
- [60] Coleman Knabe, Bryce Lee, Viktor Orekhov, and Dennis Hong. Design of a Compact, Lightweight, Electromechanical Linear Series Elastic Actuator. *Volume 5B: 38th Mechanisms and Robotics Conference*, page V05BT08A014, 2014.
- [61] Shuuji Kajita, Fumio Kanehiro, Kenji Kaneko, Kazuhito Yokoi, and Hirohisa Hirukawa. The 3D linear inverted pendulum model: a simple modeling for biped walking pattern generation. *the 2001 Intelligent Robots and Systems (IRIEEE/RSJ International Conference on*, 1(October 2016):239–246, 2011.
- [62] Sung Hee Lee and Ambarish Goswami. Ground reaction force control at each foot: A momentum-based humanoid balance controller for non-level and non-stationary ground. In *Intelligent Robots and Systems (IROS), IEEE/RSJ International Conference on*, pages 3157–3162, 2010.
- [63] Patrick M Wensing and David E Orin. Generation of dynamic humanoid behaviors through task-space control with conic optimization. In *Robotics and Automation (ICRA), IEEE International Conference on*, pages 3103–3109, 2013.
- [64] Alexander Herzog, Ludovic Righetti, Felix Grimmering, Peter Pastor, and Stefan Schaal. Balancing experiments on a torque-controlled humanoid with hierarchical inverse dynamics. *Intelligent Robots and Systems (IRIEEE/RSJ International Conference on*, (Iros):981–988, 2014.
- [65] Luis Sentis and Oussama Khatib. Synthesis of Whole-Body Behaviors Through Hierarchical Control of Behavioral Primitives. *International Journal of Humanoid Robotics*, 2(4):505–518, 2005.
- [66] Johannes Engelsberger, Christian Ott, Maximo A. Roa, Alin Albu-Schaffer, and Gerhard Hirzinger. Bipedal walking control based on capture point dynamics. *Intelligent Robots and Systems (IRIEEE/RSJ International Conference on*, pages 4420–4427, 2011.
- [67] Peter I. Corke. *Robotics, Vision & Control: Fundamental Algorithms in MATLAB*. Springer, second edition, 2017. ISBN 978-3-319-54413-7.

- [68] N. Koenig and A. Howard. Design and use paradigms for gazebo, an open-source multi-robot simulator. In *Intelligent Robots and Systems (IROS), IEEE/RSJ International Conference on*, pages 2149–2154, 2004.
- [69] Engineer’s Edge. Coefficient of friction equation and table chart.

Appendix A

2017 IEEE/RAS International
Conference on Humanoid Robots

Online Estimation of Friction Constraints for Multi-Contact Whole Body Control

Cameron P. Ridgewell¹, Robert J. Griffin^{1,2}, Tomonari Furukawa¹, and Brian Lattimer³

Abstract— This paper proposes a technique for experimentally approximating surface friction coefficients at contact-time in multi-contact applications. Unlike other multi-contact formulations, our approach does not assume a standard friction coefficient, and instead induces slip in a multi-contact oriented humanoid to estimate available friction force. Incrementally increased tangential force, measured with ankle-mounted force-torque sensors, is used as the basis for slip detection and friction coefficient estimation at the hand. This technique is validated in simulation on a simple three-link model and extended to the humanoid robot platform ESCHER. Approximated friction values are utilized by the robot’s whole body controller to prevent multi-contact end effector slip.

I. INTRODUCTION

Biomimetic robotics research continues to sophisticate the locomotive capacity of humanoid robots, but still falls vastly short of the potential of the platform, even in controlled laboratory settings. Humans are capable of traversing complex, rubble-strewn environments in a matter of seconds, while our best humanoid robots struggle to perform the same task in hours. The superiority of humans is due largely to our ability to adaptively utilize our limbs for balance in dynamic and unstructured environs, supporting ourselves with not only our legs and feet, but also our arms and hands. Inclusion of these multi-contact tripedal and quadrupedal modes allows humans to perform lateral force control easily, and even to use our hands to alleviate the required lifting force at the feet. In order to integrate this biomimetic functionality into humanoids, it is necessary to begin formulation of accurate environmental parameters. Ignoring active knowledge of friction parameters endangers the system, as an unprepared robot will invariably encounter a low-friction surface in the real world, which can cause slips and falls [1]. However, measuring or even estimating these contact properties is not always easy to do remotely or in person; indeed, small debris that would likely cause slip behaviors is not always possible to detect before making contact, even for humans [2].

The regulation of linear and angular momentum has proven key to maintain bipedal balance, with direct control provided through the environmental contact forces [3].

*This work was supported by The Office of Naval Research, Grant N00014-15-1-2128

¹The authors are associated with the Terrestrial Robotics Engineering and Controls (TREC) Laboratory at Virginia Tech, 635 Prices Fork Rd, Blacksburg, VA 24060, United States

²The authors are associated with the Florida Institute for Human and Machine Cognition, 40 S Alcaniz St, Pensacola, FL 32502, United States

³The authors are associated with the Jensen Hughes, 2020 Kraft Drive, Suite 3020, Blacksburg, VA 24060, United States

Email: (cameron.ridgewell, tomonari)@vt.edu, rgriffin@ihmc.us, blattimer@jensenhughes.com

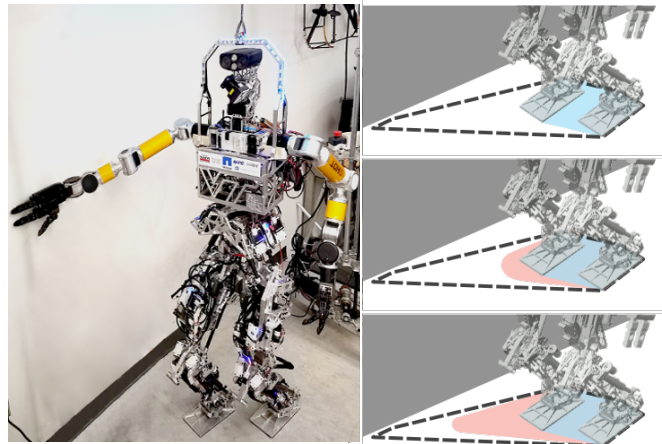


Fig. 1: The base region (blue) of the 2D static support polygon may be significantly increased (red) with the addition of a hand-support point, depending on the force limits and friction constraints (middle, bottom).

Though a variety of methods exist for finding suitable contact forces, inverse dynamics through convex optimization has proven to be a particularly powerful tool to satisfy the redundant tasks present in whole-body locomotion behaviors [4], [5]. However, the inverse dynamics approach proposed by [6] is predicated on the assumption that the contact forces used to produce the desired momentum are all achievable by their respective end effectors. This was specifically enforced in [7] by using a convex friction cone constraint with a set of local contact points representative of the net force applied at the contact surface. The established methodology for humanoid locomotion has included friction consideration to some extent, but a prescribed frictional coefficient has thus far generally been thought of as sufficient to induce adaptive gait behaviors as in [8] or reflexive recovery strategies, such as [2], [9].

A number of implementations of multi-contact behaviors have considered friction constraints, which can generally be separated into one of two categories. The first group explores friction boundaries, but assumes that the necessary friction parameters are either known or guessed for the particular execution, and therefore all motion may be completed without slip, as in [10–12]. Though this prior knowledge of the surface is ideal, friction coefficients can vary in practice due to changes in texture, moisture, or a host of other factors that limit the specificity of assumed friction values, rendering such knowledge potentially inaccurate.

The second group chooses to avoid the issues associated with potential slip conditions by utilizing either specific motion planning or whole body control weighting methods

to produce forces only in the normal direction at the hands [13]. Though it is not unreasonable to use either exclusively normal forces or an extremely conservative friction cone to reduce the likelihood of slip behaviors in foot placement on level terrain, since multi-contact movements often include non-gravity-normal contact points, which are generally used in conjunction with tangential force, it becomes necessary to either actively establish friction parameters at the point of contact or else risk both slip and unnecessary restriction of the support region. Thus far, no reliable method has emerged to actively sense friction parameters at the hands in order to fully exploit available tangential forces in continued use in multi-contact scenarios.

In this work, we propose a technique for online determination of static friction for hand placement in multi-contact scenarios to address the uncertainty associated with the friction coefficients. An initially conservative coefficient of friction is used to establish contact, and then, by providing an end effector wrench of increasing load, slip is induced at the contact point. These actions are performed while maintaining the overall balance of the robot, and Coulomb's Law of Friction is used to extrapolate the surface's static friction coefficient, which is utilized in the whole body controller's friction cone representation of the contact point. The advantages of this approach are that it requires no additional sensors, other than those present on most bipedal platforms, and may potentially provide accurate estimates of friction parameters in the field, allowing humanoid platforms to avoid multi-contact slip.

This paper is constructed as follows: first the underlying formulations the whole body control framework and its friction constraints are introduced. We then explain the methodology for determining contact slip and the technique for measuring and integrating the coefficient of friction at execution time. A simple model simulating this principle is presented to demonstrate the validity of the approach. Finally, the technique is validated experimentally on the ESCHER robot platform [14], followed by a discussion of the implications of this experimental procedure for determination of frictional constraints.

II. MULTI-CONTACT BALANCING WITH FRICTION CONSIDERATIONS

In this section, we review the robot's rigid body dynamic formulation, summarize the whole-body controller presented in [15], and provide an explanation of friction constraints in the controller's task space model optimization.

A. Floating-Base Humanoid Dynamics

The rigid body dynamics of an articulated humanoid with n actuated degrees of freedom (DoF) can be described by the vector \mathbf{q} , where $\mathbf{q} = [\mathbf{q}_0^T \quad \mathbf{q}_n^T]^T \in \mathbb{R}^{6+n}$ such that $\mathbf{q}_0 \in \mathbb{R}^6$ represents the location and orientation of the floating base and $\mathbf{q}_n \in \mathbb{R}^n$ is the vector of robot joint angles. The floating-base rigid body equation is given as

$$\begin{bmatrix} \mathbf{0} \\ \boldsymbol{\tau} \end{bmatrix} = \mathbf{H}(\mathbf{q})\ddot{\mathbf{q}} + \mathbf{C}(\mathbf{q}, \dot{\mathbf{q}}) - \sum_c \mathbf{J}_c^T \mathbf{f}_c, \quad (1)$$

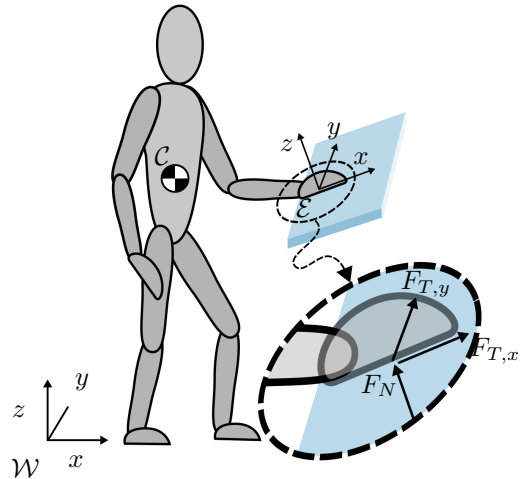


Fig. 2: Illustration of humanoid robot contact frames.

where $\boldsymbol{\tau} \in \mathbb{R}^n$ is the vector of joint torques, $\mathbf{H} \in \mathbb{R}^{6+n}$ is the joint-space inertia matrix, and $\mathbf{C} \in \mathbb{R}^{6+n}$ is the vector of centrifugal, Coriolis, and gravity torques. Each $\mathbf{f}_c \in \mathbb{R}^6$ is a wrench vector of external forces and torques corresponding to contact body c with corresponding Jacobian, \mathbf{J}_c . For example, a humanoid platform could have four bodies in contact ($c = 4$),

$$\begin{bmatrix} \mathbf{f}_1^T \\ \mathbf{f}_2^T \\ \mathbf{f}_3^T \\ \mathbf{f}_4^T \end{bmatrix} = \begin{bmatrix} \mathbf{f}_{\text{foot},l}^T \\ \mathbf{f}_{\text{foot},r}^T \\ \mathbf{f}_{\text{hand},l}^T \\ \mathbf{f}_{\text{hand},r}^T \end{bmatrix}, \quad (2)$$

where each external force vector is a six-element vector of the associated link forces and torques, $[F_x, F_y, F_z, M_x, M_y, M_z]^T$. These individual force elements are represented in the end effector frame of the contact link as in Figure 2, and mapped to the inertial frame via \mathbf{J}_c .

B. Principles of Friction

Coulomb friction dictates that slip will not occur when the tangential force is less or equal to than the available frictional force between two objects,

$$F_T \leq \mu_s F_N, \quad (3)$$

where F_T is magnitude of tangential force, μ_s is the coefficient of static friction, and F_N is the normal force between the two objects. Based on this representation, the static friction coefficient can be determined through the relationship between normal and tangential forces in the maximally loaded no-slip condition, when F_T is equal to the available frictional force. Given this relationship, the end effector reference frame can be placed such that the normal force is parallel to the z -axis, making the tangential force a vector in the x - y plane of the end effector, as in Figure 2.

C. Convex Friction Cone Constraint

The frictional constraints on the contact forces can be described using a convex second order cone constraint,

$$f_{c,x}^2 + f_{c,y}^2 < (\mu_s f_{c,z})^2, \quad (4)$$

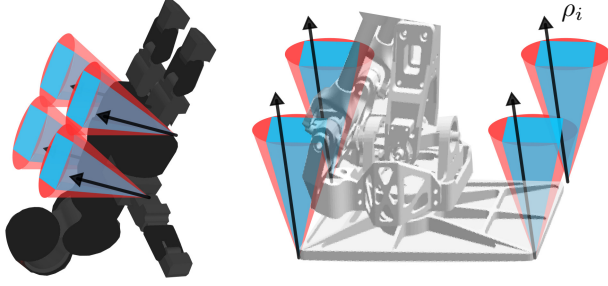


Fig. 3: Friction cone and friction pyramid distributed representations of localized end effector contact points on palm (left) and foot (right).

as shown with the friction cones in Figure 3. This, however, has the disadvantage of requiring a quadratic constraint. Instead, the friction cone can be conservatively described using an inscribed pyramid, comprised of m basis vectors $\mathbf{B}_{c,m}$ [5], [7],

$$\mathbf{f}_c = \sum_m \mathbf{B}_{c,m} \rho_{c,m}, \quad (5)$$

where $\rho_{c,m}$ is the generalized contact force along vector m at contact point c . This has the advantage of reducing the frictional constraint to the linear domain, enabling much faster solution approaches. This constraint then ensures that the force \mathbf{f}_c always lies within the friction cone.

D. Task Space Model Optimization

The inverse dynamics approach presented in [15] can be used to solve for the desired generalized contact forces, $\boldsymbol{\rho} = [\rho_1^T \dots \rho_N^T]^T$ and joint accelerations, $\ddot{\mathbf{q}}$, through minimization of the quadratic cost function

$$\min_{\ddot{\mathbf{q}}, \boldsymbol{\rho}} \|\mathbf{C}_b(\mathbf{b} - \dot{\mathbf{J}}\ddot{\mathbf{q}} - \mathbf{J}\ddot{\mathbf{q}})\|^2 + \lambda_{\ddot{\mathbf{q}}} \|\ddot{\mathbf{q}}\|^2 + \lambda_{\boldsymbol{\rho}} \|\boldsymbol{\rho}\|^2 \quad (6)$$

subject to the equality and inequality constraints:

$$\dot{\mathbf{A}}\ddot{\mathbf{q}} + \mathbf{A}\ddot{\mathbf{q}} = \sum_c \mathbf{W}_c \mathbf{f}_c + \mathbf{w}_g \quad (7)$$

$$\underline{\mathbf{q}} \leq \mathbf{q} + T\dot{\mathbf{q}} + \frac{1}{2}T^2\ddot{\mathbf{q}} \leq \bar{\mathbf{q}} \quad (8)$$

$$\underline{\boldsymbol{\tau}} \leq \boldsymbol{\tau} \leq \bar{\boldsymbol{\tau}} \quad (9)$$

$$\mathbf{0} \leq \boldsymbol{\rho} \quad (10)$$

where \mathbf{C}_b is representative of the task weighting matrix such that $\mathbf{Q}_b = \mathbf{C}_b^T \mathbf{C}_b$ is the positive definite weight matrix, \mathbf{b} is the vector of desired motion tasks, and $\lambda_{\ddot{\mathbf{q}}}$ and $\lambda_{\boldsymbol{\rho}}$ are regularization parameters. In this case, the matrix \mathbf{W}_c encodes both \mathbf{J}_c and \mathbf{B}_c for each contact point, ensuring the frictional constraint in Equation 5. Note that, from the rigid body dynamics in Equation 1, torque can be included as a linear function of the joint accelerations and generalized contact forces, and does not need to be explicitly solved for.

III. ONLINE APPROXIMATION OF CONTACT POINT FRICTION COEFFICIENTS

We now present our method for multi-contact slip detection by describing our method for determining friction coefficient by approximating hand contact forces in concurrence with Coulomb's Law.

A. Slip Detection

Our proposed technique induces a lateral slip on the contact surface in order to approximate μ_s with Coulomb Friction law. We assume dry, uniform surface friction at the palm, and measure indirectly both F_N and F_T at the surface. Maximum tangential stiction force prior to slip, as demonstrated in [16], is a reliable indicator of stick-slip behavior, and therefore maximum static friction force. However, since a change in F_T will indicate when slip has already occurred, our approach records the previously measured values of tangential force in order to accurately estimate μ_s . So, for any set of recorded discrete loadings of increasing F_T with time step t ,

$$\mu_s = \frac{\max(F_{T,t})}{F_{N,t}}. \quad (11)$$

B. Static Friction Approximation

In order to estimate slip via applied forces at the hand, the proposed approach utilizes the disturbance approximation equation developed in [17] to detect external force for robots with force-torque sensors in contact with the ground

$$M\ddot{\mathbf{x}}_{\text{cog}} = {}^{\text{cog}}\mathbf{T}_c \mathbf{f}_c + {}^{\text{cog}}\mathbf{T}_{\text{dist}} \mathbf{f}_{\text{dist}} + M\mathbf{g} \quad (12)$$

where M is the mass of the robot, ${}^{\text{cog}}\mathbf{T}_c$ and ${}^{\text{cog}}\mathbf{T}_{\text{dist}}$ are the homogeneous transforms from the contact frame and disturbance frame to the center of gravity (CoG) frame, respectively, \mathbf{f}_{dist} is some disturbance force, and \mathbf{g} is the gravity vector. If it is assumed no additional forces are applied during the friction measurement process, this equation can be reformulated to calculate any unknown contact force, for example a single additional contact with the hand, \mathbf{f}_{hand} ,

$$\mathbf{f}_{\text{hand}} = {}^{\text{hand}}\mathbf{T}_{\text{cog}}(M(\ddot{\mathbf{x}}_{\text{cog}} - \mathbf{g}) - {}^{\text{cog}}\mathbf{T}_{\text{foot},l} \mathbf{f}_{\text{foot},l} - {}^{\text{cog}}\mathbf{T}_{\text{foot},r} \mathbf{f}_{\text{foot},r}) \quad (13)$$

where $\mathbf{f}_{\text{foot},l}$ and $\mathbf{f}_{\text{foot},r}$ are the measured force values of the left and right foot respectively. Applying the appropriate transformation between the end effector contact frames and the center of gravity frame \mathcal{C} , the coefficient of static friction may be determined using an increasing contact force by combining Equations 11 and 13,

$$\mu_s = \frac{\max(S_T \mathbf{f}_{\text{hand}})}{S_N \mathbf{f}_{\text{hand}}} \quad (14)$$

where \mathbf{S}_T and \mathbf{S}_N are selection matrices for the tangential and normal forces, respectively. Solving for this equation, the resulting μ_s is used to generate the friction cone used to find the basis vectors $\mathbf{B}_{i,\text{hand}}$ in Equation 5. By performing this brief technique at the time of contact, assuming contact is initiated in a purely normal direction, slip can be reliably avoided through friction coefficient approximation.

IV. SIMULATED FRICTION APPROXIMATION

In order to verify this methodology for friction estimation, Algorithm 1 was developed to approximate the force applied at the hands using only the force-torque sensors at the base. Desired applied normal force, $F_{N,d}$ is specified while the tangential force $F_{T,d}$ is incremented by step size, k , where $\mathbf{f}_{e,d}$ and $\mathbf{f}_{e,m}$ delineate the desired and measured forces at the end effector(s), respectively. With the development of this functionality, the algorithm was applied on two separate systems.

Algorithm 1 Incremental Friction Approximation

```

1: procedure FRICTIONAPPROX( $F_{N,d}, k$ )  $\triangleright$  estimate  $\mu_s$ 
2:    $F_{T,max} = 0$ 
3:   do
4:      $F_{T,d} = F_{T,d} + k$   $\triangleright$  increment  $F_{T,d}$  by  $k$ 
5:      $\mathbf{f}_{e,d} = [0 \ F_{T,d} \ F_{N,d} \ 0 \ 0 \ 0]$ 
6:     whole_body_controller.set( $\mathbf{f}_{e,d}$ )
7:     update_sensors()  $\triangleright$  update  $\ddot{\mathbf{x}}$  and  $\mathbf{f}_{base,m}$ 
8:      $\mathbf{f}_{e,m} = {}^e\mathbf{T}_{cog}(M\ddot{\mathbf{x}} - {}^{cog}\mathbf{T}_b\mathbf{f}_{base,m} - Mg)$ 
9:      $F_{T,m} = \mathbf{f}_{e,m,tangential}$ 
10:     $F_{N,m} = \mathbf{f}_{e,m,normal}$ 
11:    while  $F_{T,m} < F_{T,max}$   $\triangleright F_{T,m} >$  than previous
12:       $\mu_s = F_{T,m} \div F_{N,m}$   $\triangleright$  Equation 11
13:    return  $\mu_s$ 

```

A. Introduction of the Three-Link Model

We consider a three-link planar robot constructed using the Robotics Toolbox [18], configured to touch a non-gravity normal plane. In humanoids, hand contacts are typically used as largely secondary balance limbs, with primary support being provided by the legs. As such, the portion of the normal force at the base foot is significantly greater than that applied at the hand. This is reflected in the three link model by limiting maximum total force at the end effector, and by considering the base link, the foot, to have sufficient total normal force to avoid slip itself. In such a case, the base joint may be considered fixed, with net force values measured at this point. For the purpose of this simulation, each link is 0.432 m long, and at an evenly-distributed 17.4 kg.

Following Algorithm 1, with an initial $F_{N,d}$ applied, the tangential force is increased from 0 N until slip is detected in increments of $k = 0.10$ N, 0.20 N, and 0.55 N. Tangential force is increased over the a 1 second period and measured at the end of the period. Slip detection is indicated by the point at which the measured $F_{T,m}$ value at the base link is less than the previous $F_{T,m}$ value, indicating a transition between the static friction and kinetic friction states, since kinetic friction force is less than its static counterpart. Once initial slip has been detected at the maximum $F_{T,m}$ value, utilizing Equation 11, the friction coefficient is approximated.

B. Simulation of Different Increment Sizes

In Figures 4a and 4b, the friction coefficients, chosen arbitrarily, are $\mu_s = 0.36125$ and $\mu_k = 0.19125$. The initial experiment, 4a shows an $F_{N,d}$ of 5 N, so slip occurs when

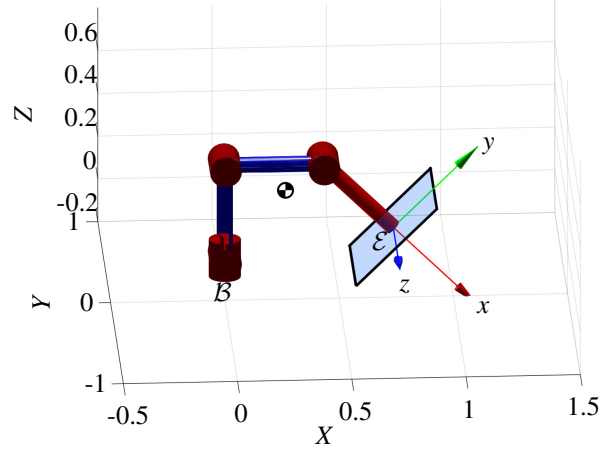


Fig. 5: A simple 3-link model was developed to simulate a robot with fixed base B pushing on a non-gravity normal surface at the end effector, E .

$F_T = 1.80625$ N. Step size is a factor in this simulation, as the higher k value ends up with a greater error (8.7%) compared to the other two smaller step sizes (0.346%). These results indicate that increasing k , the rate at which F_T is increased, causes the algorithm less accurate than use of a smaller k , though small k values have a longer execution time.

C. Increasing the Desired Normal Force

To counter the inaccuracies of a high k , in the second simulation, Figure 4b, the normal force is increased to 20 N, therefore increasing the magnitude of the slip value for F_T . The resultant measurements are generally more accurate, (0.346%, 0.346%, and 1.03% error for $k = 0.1, 0.2,$ and 0.55 respectively). While this increased normal force causes the larger step size to be more accurate, all of the step sizes take more time than in the previous simulation. It is also worth noting that, in this paper's proposed application, use of large forces at the hand contact can lead to potentially dangerous results when slip does occur, with the resulting imbalance affecting the entire system.

D. Approximation with Similar Coefficients

For the third simulation, Figure 4c, the normal force is returned to 5 N, but the friction values are changed to $\mu_s = 0.30020$ and $\mu_k = 0.25001$. The proximity of μ_s and μ_k limits the maximum error of the system, but the results indicate that increasing step size leads to less accurate approximate friction values (0.067%, 6.73%, and 16.7% error for $k = 0.1, 0.2,$ and 0.55 respectively). While step size is not the primary factor in this process, these results indicate that raising F_T too quickly causes inaccuracies in the measured values. It is worth noting that, due to the relationship between static and kinetic frictional forces, Algorithm 1 should never overestimate the frictional value of the surface, though the magnitude of its underestimation may be largely dependent on the difference between μ_s and μ_k .

V. EXPERIMENTAL RESULTS WITH ESCHER PLATFORM

The method presented in Algorithm 1 and Equation 14 was utilized on ESCHER, a full size compliant humanoid

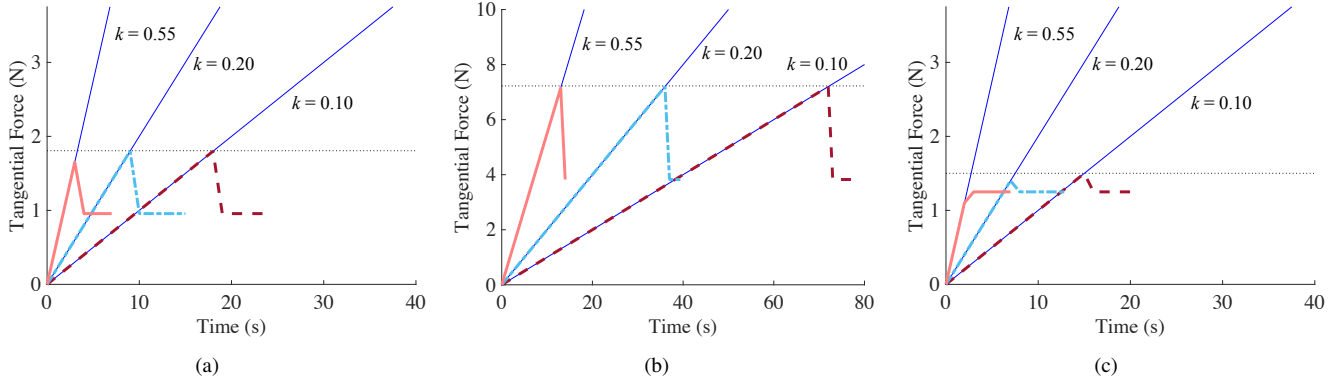


Fig. 4: The tangential element of the applied f_c continues along the blue line, but the red line shows the measured F_T at the base link. The horizontal dotted line indicates the proper location of slip, which may be under- or over-shot depending on the step increment size, the magnitude of normal force, and the actual coefficients of friction of the system. The value $F_T = \mu_s F_N$ is denoted by the horizontal dotted line.

robot developed by the Virginia Polytechnic Institute and State University for use in the DARPA Robotics Challenge [14]. ESCHER has 38 DoF, with 6 DoF in each leg, 7 DoF in each arm, and an additional 3 DoF in each hand. The robot stands 1.8 m tall and weighs 77 kg when operating with batteries enclosed in the chest compartment, but only 70 kg when operated with an external power supply. Though many proprioceptive sensors are contained on this platform, those of most important note are the ankle-mounted ATI Mini-58 six-axis force/torque transducers, used to measure ground contact and reaction forces of each foot [14].

A. Friction Estimation on Simulated ESCHER

Friction coefficient estimation is established as a user-enacted module communicating with the robot’s momentum controller and operating system. When standing, the robot, already in a multi-contact pose utilizing exclusively normal force at its hand, is prompted to estimate the friction coefficient by iterative escalation of F_T applied at its hand, as in Algorithm 1. This tangential force, provided as an objective to the whole body controller, is monitored via the ankle force torque sensors. After a peak F_T is achieved, followed by the characteristic dip demonstrated in the data from Figure 4, the slip condition is fulfilled. To prevent false maximums in F_T , measurement continues for 3.5 seconds after the approximated maximum value.

The proposed method, in accordance with Equations 13 and 14, estimated static friction force to act as the friction limit for the optimization Equation 5, expanding the friction cone beyond its conservative initial value. As noted in [17], derivation of \ddot{x}_{cog} from exclusively the joint positions of the platform can result in excessive noise. To counter this, the momentum rate of change of the ESCHER momentum controller is estimated from an equal fusion of the Kalman-filtered acceleration vector from the onboard inertial measurement unit (IMU), located at the pelvis, and the calculated CoG acceleration derived from the joint states and rigid body dynamics of the system. The data received from the force-torque sensors was processed through a low-pass filter to limit signal noise.

B. Friction Estimation with ESCHER in Gazebo

The simulated model of ESCHER was placed in a Gazebo Simulation [19] and navigated to a position 1.0 m behind a box of height 1.2 m. The actual friction coefficient between the box and the robot’s hand was set to $\mu_s = 0.50$. The proposed estimation technique was applied, with results shown in Figure 7. With the increased imprecision of the 38 DoF system, there was noticeable noise, as well as the beginnings of stick-slip behavior in the resulting measured F_T . With a step size k of 0.5 N, the maximum measured F_T , 7.04 N, occurred just after 4 seconds, when the F_N , set to 15 N, was measured at 14.64 N. The estimated value of $\mu_s = 0.481$ was 3.8% lower than the actual value of 0.5. As can be seen in the bottom of Figure 7, the coefficient of friction is continuously recalculated as F_T is increased, with its maximum value dependent on the peak F_T . Though there are some limitations to accuracy with this relatively low F_N , the goal of preventing slip is realized as, due to the consistent relationship between static and kinetic friction, the proposed approach will tend toward accuracy without exceeding the actual μ_s . This allows ESCHER to avoid slips at hand contacts due to overestimated friction forces.

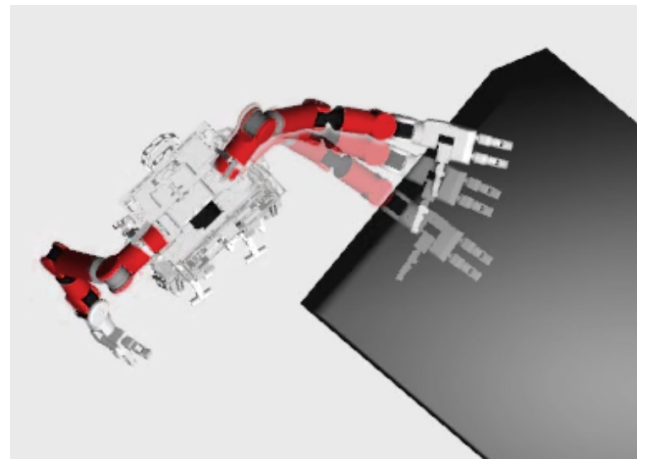


Fig. 6: The tangential force is applied in laterally along the end effector y axis, allowing the robot’s hand to slide over the contact surface when the friction force is exceeded.

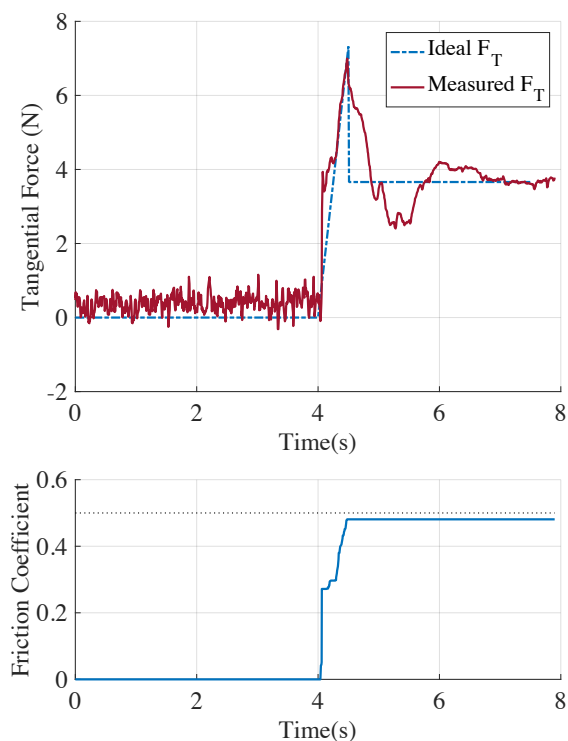


Fig. 7: In the ESCHER Simulation, the maximum F_T achieved was 7.04 N (top). Though the setpoint force for F_N force was 15 N, at the maximum value of F_T , just before 4.5 s, the normal force was measured at, 14.64 N. The calculated friction coefficient, starting at $\mu_s = 0$, was approximated based on the $F_{T,max}$ to $\mu = 0.481$ (bottom), compared to the actual value, 0.500

VI. CONCLUSION

Complex environments demand high maneuverability from humanoid platforms lacking complete knowledge of their surroundings. Though conservative approximation may provide a base maneuverability to the platform, it will always tread the line between risking the robot's balance and unnecessarily constricting its movement. In this paper we proposed an additional tool for a humanoid platform to analytically explore its environment, providing more certain hand holds for reliable whole body control.

The applications shown above provide proof-of-concept that this technique may be utilized as a method for extrapolating friction information at sensor-less end effectors. Though accuracy is largely dependent on step size and sensor accuracy, the data provided here point to the validity of this technique. Future work will include utilizing the functionality on the ESCHER platform to verify its physical accuracy and significance. Accurate physical characterization of friction parameters could expand the robot's breadth of multi-contact applications which might be extended to include dynamic support during hand sliding maneuvers.

The in-field utility of this technique is questionable if the time required becomes significant, as taking several seconds to test every surface in a proposed environment may be a costly endeavor. However, since many surfaces in any environment are frequently similar, collected knowledge of the environment would likely provide a better starting point

for test values of μ_s . To this end, the friction measurement technique could be extended to include vision-based machine learning to improve the starting parameters for measurement.

ACKNOWLEDGMENT

This work was supported by the Office of Naval Research, Grant N00014-15-1-2128 as part of development of Project SAFFiR (Shipboard Autonomous Firefighting Robot). The authors would also like to recognize the support of DARPA's support during the 2015 DARPA Robotics Challenge.

REFERENCES

- [1] J. A. Vázquez and M. Velasco-Villa, "Experimental estimation of slipping in the supporting point of a biped robot," *Journal of Applied Research and Technology*, vol. 11, no. 3, pp. 348–359, 2013.
- [2] G. N. Boone and J. K. Hodgins, "Slipping and tripping reflexes for bipedal robots," *Autonomous Robots*, vol. 4, no. 3, pp. 259–271, 1997.
- [3] A. Macchietto *et al.*, "Momentum control for balance," in *ACM Transactions on Graph. (TOG)*, vol. 28, no. 3. ACM, 2009, p. 80.
- [4] B. J. Stephens and C. G. Atkeson, "Dynamic Balance Force Control for Compliant Humanoid Robots," in *Intelligent Robots and Systems (IROS), 2010 IEEE/RSJ Int. Conf. on*, 2010, pp. 1248–1255.
- [5] S. H. Lee and A. Goswami, "Ground reaction force control at each foot: A momentum-based humanoid balance controller for non-level and non-stationary ground," in *Intelligent Robots and Systems (IROS), 2010 IEEE/RSJ Int. Conf. on*, 2010, pp. 3157–3162.
- [6] J. Park and O. Khatib, "Contact consistent control framework for humanoid robots," in *Robotics and Automation (ICRA), 2006 IEEE Int. Conf. on*, no. 1, 2006, pp. 1963–1969.
- [7] P. M. Wensing and D. E. Orin, "Generation of dynamic humanoid behaviors through task-space control with conic optimization," in *Robotics and Automation (ICRA), 2013 IEEE Int. Conf. on*, 2013, pp. 3103–3109.
- [8] S. Kajita *et al.*, "Biped walking on a low friction floor," in *Intelligent Robots and Systems (IROS), 2004 IEEE/RSJ Int. Conf. on*, 2004, pp. 3546–3552.
- [9] K. Ohung and J. H. Park, "Reflex control of bipedal locomotion on a slippery surface," *Advanced Robotics*, vol. 16, no. 8, pp. 721–734, 2002.
- [10] L. Sentis *et al.*, "Compliant control of multicontact and center-of-mass behaviors in humanoid robots," *IEEE Transactions on Robotics*, vol. 26, no. 3, pp. 483–501, 2010.
- [11] O. Khatib and S. Y. Chung, "SupraPeds: Humanoid contact-supported locomotion for 3D unstructured environments," in *Robotics and Automation (ICRA), 2014 IEEE Int. Conf. on*, 2014, pp. 2319–2325.
- [12] E. Farniolil *et al.*, "Toward Whole-Body Loco-Manipulation : Experimental Results on Multi-Contact Interaction with the Walk-Man Robot," in *Intelligent Robots and Systems (IROS), 2016 IEEE/RSJ Int. Conf. on*, 2016, pp. 1372–1379.
- [13] B. Henze *et al.*, "Posture and balance control for humanoid robots in multi-contact scenarios based on Model Predictive Control," in *Intelligent Robots and Systems (IROS), 2014 IEEE/RSJ Int. Conf. on*, 2014, pp. 3253–3258.
- [14] C. Knabe *et al.*, "Team VALOR's ESCHER: A Novel Electromechanical Biped for the DARPA Robotics Challenge," *Journal of Field Robotics*, vol. 34, no. 2, pp. 1–28, 2017.
- [15] M. A. Hopkins *et al.*, "Compliant locomotion using whole-body control and Divergent Component of Motion tracking," in *Robotics and Automation (ICRA), 2015 IEEE Int. Conf. on*, 2015, pp. 5726–5733.
- [16] R. Bayrleithner and K. Komoriya, "Static friction coefficient determination by force sensing and its application," in *Intelligent Robots and Systems (IROS), 1994 IEEE/RSJ Int. Conf. on*, vol. 3, 1994, pp. 1639–1646.
- [17] K. Kaneko *et al.*, "Disturbance observer that estimates external force acting on humanoid robots," *Advanced Motion Control (AMC), 2012 12th IEEE Int. Workshop on*, pp. 1–6, 2012.
- [18] P. I. Corke, *Robotics, Vision & Control: Fundamental Algorithms in MATLAB*, 2nd ed. Springer, 2017, ISBN 978-3-319-54413-7.
- [19] N. Koenig and A. Howard, "Design and use paradigms for gazebo, an open-source multi-robot simulator," in *Intelligent Robots and Systems (IROS), 2004 IEEE/RSJ Int. Conf. on*, 2004, pp. 2149–2154.